Photocatalytic degradation of antibiotic and hydrogen production using diatom-templated 3D WO3-x@mesoporous carbon nanohybrid under visible light irradiation

Gholami, Peyman

2020-12-01

Gholami , P , Khataee , A & Bhatnagar , A 2020 , ' Photocatalytic degradation of antibiotic and hydrogen production using diatom-templated 3D WO3-x@mesoporous carbon nanohybrid under visible light irradiation ' , Journal of Cleaner Production , vol. 275 , 124157 . https://doi.org/10.1016/j.jclepro.2020.124157

http://hdl.handle.net/10138/351287
https://doi.org/10.1016/j.jclepro.2020.124157

acceptedVersion

Photocatalytic degradation of antibiotic and hydrogen production using diatom-templated 3D WO_{3-x}@mesoporous carbon nanohybrid under visible light irradiation

Peyman Gholami, [a,b,c] Alireza Khataee, [a,d,e,*] Amit Bhatnagar[b]

[a] Research Laboratory of Advanced Water and Wastewater Treatment Processes, Department of Applied Chemistry, Faculty of Chemistry, University of Tabriz, 51666-16471 Tabriz, Iran

[b] Department of Environmental and Biological Sciences, University of Eastern Finland, P.O. Box 1627, FI-70211 Kuopio, Finland

[c] Department of Chemistry, University of Helsinki, P.O. Box 55, Helsinki 00014, Finland

[d] Department of Environmental Engineering, Gebze Technical University, 41400 Gebze, Turkey

[e] Institute of Research and Development, Duy Tan University, Da Nang 550000, Vietnam

* Corresponding authors:

a_khataee@tabrizu.ac.ir (A. Khataee)

Abstract

Synthesis of highly efficient 3D photocatalysts offers unique abilities for hydrogen production and chemical conversion to find a solution for energy shortage and environmental pollution issues. However, current strategies for production of ordered nanohybrid photocatalysts usually involve complex procedures and the use of expensive templates, which limit their practical applications. In this work, 3D WO_{3-x}@mesoporous carbon photocatalyst was fabricated through one-pot evaporation-induced self-assembly (EISA) process using *Cyclotella sp.* as natural template. During heat-treatment, the precursor of carbon could partially reduce tungsten oxide under N_2 atmosphere leading to the embedding of WO_{3-x} in conductive mesoporous carbon structure. The diatom templated WO_{3-x}@mesoporous carbon (DT-WO_{3-x}@MC) nanohybrid exhibited high surface area (195.37 m^2 g^{-1}) and narrowed band gap (2.67 eV). Integration of tungsten oxide with mesoporous carbon and formation of oxygen vacancies enhanced the absorption of visible light using DT-WO_{3-x}@MC and limited the recombination of electron-hole pairs. 98.7% of cefazolin (CFZ) degradation efficiency and 85.5% of total organic carbon (TOC) removal efficiency were observed within 90 and 180 min under visible light irradiation, respectively. Scavenger quenching tests and electron spin resonance (ESR) analysis demonstrated that $O_2^{\bullet-}$ played a main role in photocatalysis. CFZ degradation pathway was proposed via identification of conversion intermediates using GC-MS analysis. Photocatalytic hydrogen production rates of the pure WO_3 and the DT-WO_{3-x}@MC nanohybrid were determined as 746 and 1851 µmol g^{-1} h^{-1}, respectively. This study presented a way to develop a high-performance and stable photocatalyst using diatom frustules as natural template which works under practical conditions for environmental remediation and energy production.

Keywords: Tungsten oxide; Diatom-templated photocatalyst; WO_{3-x}@mesoporous carbon; Photocatalysis; Antibiotic degradation; Hydrogen production.

1. Introduction

Fast industrialization and urbanization has caused a remarkable increase in non-renewable energy consumption depleting energy sources as well as discharging toxic contaminants in environment (Kumar *et al.* 2018; Mir & Pandey 2019; Singh *et al.* 2019; Cha-Umpong *et al.* 2020; Kobya *et al.* 2020). To meet the environmental challenges and enhance the exploitation of renewable energy resources, photocatalytic production of hydrogen (H_2) energy has gained great attention (Liu et al. 2019). Furthermore, antibiotics residues from aquaculture, hospital effluent, and livestock or humans medicines have been widely detected in water bodies (Teodosiu et al. 2018; Patel et al. 2019). The misuse of antibiotic medications has resulted in serious environmental pollution and human health hazards (Chen et al. 2019; Zhang et al. 2020a).

Various semiconductors such as metal oxides, sulfides, oxysulfide, heterojunctions and layered double hydroxides have been widely investigated for the photocatalytic H_2 evolution and photodegradation of different pollutants under light irradiation (Li *et al.* 2018b; Wang *et al.* 2019; Gholami *et al.* 2020b; Hu *et al.* 2020). But due to their large band gaps, they are only excited by ultraviolet (UV) light (wavelengths less than 400 nm), that merely occupies about 3–5% in sunlight (Li et al. 2018a).

Tungsten trioxide (WO_3), an n-type photocatalyst with an energy band gap (E_g) of ~2.8 eV, has gained great attention among the semiconductor photocatalyst materials owing to its nontoxicity, unique physicochemical characteristics, low-cost and high stability (Žerjav *et al.* 2017; Cai *et al.* 2019). Nevertheless, pure WO_3 has low efficacy for energy conversion because of insufficient reduction potential and fast recombination of charge carriers (Jamila et al. 2020). According to literature, photocatalytic activity of WO_3 can be improved by incorporation of carbon materials (Phang & Tan 2019; Jamila et al. 2020). Furthermore, O vacancy in WO_{3-x}

serves as shallow donor to increase the electrical conductivity, donor density, and the surface species adsorption (Guo et al. 2019). For instance, Dong et al. have demonstrated that WO_{3-x}/2D g-C_3N_4 photocatalyst benefits from introduction of oxygen vacancy in WO_{3-x} and exfoliation of g-C_3N_4 to show the superior photocatalytic performance for removing antibiotic, organic dye and bacteria from water (Dong et al. 2020).

The synthesis of photocatalysts with the best performing morphology and nano-size pore structure faces aggregation/agglomeration problems, which can reduce photocatalytic activity by decreasing surface active sites and light adsorption and encouraging particles settling (Gora & Andrews 2019). To overcome this complication and enhance the restricted characteristics of synthesized nanomaterials, a feasible approach is required to produce the complex three-dimensional (3D) structures with precisely controlled and well-defined morphologies (Lee et al. 2018; Li et al. 2019a). Application of a natural template to fabricate inexpensive and ordered nanostructures with controlled size and morphology is a particularly interesting realm. Single cell diatoms could be considered as an attractive template to synthesize 3D structures (Ragni *et al.* 2018; Li *et al.* 2019a; Sriram *et al.* 2020). One of the special properties of these microorganisms is their 3D silica cell wall (frustule), which can provide ordered and complex pore patterns. These unique 3D silica structures are not feasible to synthesize by existing technologies (Ragni et al. 2018).

To the best of authors' knowledge, there has been no previous report on the fabrication of 3D WO_{3-x}/mesoporous carbon (WO_{3-x}@MC) nanohybrid using environmentally non-toxic and abundantly available diatom template. The effective removal of the antibiotics is of great significance to the environment due to their non-biodegradability and toxic effects (Chen *et al.* 2019; Acharya *et al.* 2020; Zhang *et al.* 2020a). Therefore, the aims of this study were to (a) fabricate diatom templated WO_{3-x}@mesoporous carbon (DT-WO_{3-x}@MC) nanohybrid with 3D structure through one-pot evaporation-induced self-assembly (EISA) method, (b)

characterize as-synthesized nanohybrid photocatalyst, and (c) evaluate its activity in photocatalytic hydrogen production and degradation of cefazolin (CFZ, a semi-synthetic β-lactam antibiotic derived from *Cephalosporium acremonium*) under visible light irradiation. Based on the results obtained from linear sweep voltammetry (LSV) response, electron spin resonance (ESR) analysis and scavenger quenching tests a possible mechanism was predicted for transportation of photo-generated charge carriers and formation of reactive species during photocatalysis.

2. Materials and Methods

2.1. Reagents and chemicals

Cyclotella sp. cells were purchased from the Iranian Biological Resource Center (Iran). Sulfuric acid (H_2SO_4, ≥ 98%), sodium hydroxide (NaOH, ≥ 98%), ethanol (C_2H_5OH, 99%), ferrous sulfate tetrahydrate ($FeSO_4.4H_2O$, 99%), ammonium formate (HCO_2NH_4, 99.9%), sodium sulphate (Na_2SO_4, 99.9%), diethyl ether ($C_4H_{10}O$, ≥99.7%), hydrochloric acid (HCl, 38%), hydrogen peroxide (H_2O_2, 30%), and N,O-bis-(trimethylsilyl)-acetamide ($C_8H_{21}NOSi_2$, ≥95%) were obtained from Merck (Germany). Phenol (C_6H_5OH, ≥ 99%), formaldehyde solution (CH_2O, 37 wt%), tetrahydrofuran (THF, C_4H_8O ≥ 99%), benzoquinone ($C_6H_4O_2$, ≥ 98%), isopropanol (C_3H_8O, 99%), acetone (C_3H_6O, 99.8%), tungsten chloride (WCl_6, 99.9%), sodium sulfide (Na_2S, 99%), sodium sulfite (Na_2SO_3, 99%), acetonitrile (C_2H_3N, HPLC grade), ethylenediaminetetraacetic acid disodium salt ($C_{10}H_{14}N_2Na_2O_8$, 99%) and disodium hydrogen phosphate (Na_2HPO_4, HPLC grade) were provided from Sigma-Aldrich (USA). Cefazolin was obtained from Loghman Co. (Iran).

2.2. Synthesis of materials

Preparation of diatom cells: To prepare nanoporous silica from *Cyclotella sp.*, the organic matrix covering the cell wall was removed using the method proposed in our previous work (Gholami et al. 2020a). H_2O_2 (60 mM) and $FeSO_4.4H_2O$ (15 mM) were added into 80 mL deionized water containing *Cyclotella sp.* (4.8×10^5 cells mL^{-1}). The suspension pH was adjusted to 3 using H_2SO_4 (0.1 M) and NaOH (0.1 M). The reaction mixture was then subjected to ultrasound irradiation for 4 h at 40 °C using an ultrasonic bath (EP S3, 40 kHz, 300 W, Sonica, Italy). The sonicated cells were separated from the liquid phase using centrifugation at 4500 rpm for 15 min. The collected white powder was washed with ammonium formate (0.5 M) and deionized water three times and dried at 10 ˚C for 24 h.

Resol precursor synthesis: A soluble resol was polymerized from phenol and formaldehyde as described previously (Yang et al. 2017b). Typically, phenol (6.10 g) was melted at 42 °C before addition of NaOH aqueous solution (1.30 g, 20%) with stirring for 10 min. Then, formaldehyde solution (10.0 g, 37%) was dropwise added into the reaction mixture and the obtained solution was mixed for 60 min at 75 °C. Subsequently, the system was cooled to ambient temperature, followed by adding 2.0 M of HCl solution to reach the pH to 7.0. Water was evaporated under vacuum condition at 45 °C and the final product was dispersed in THF (20 wt%).

Synthesis of diatom templated WO_{3-x}@MC (DT-WO_{3-x}@MC): a suspension containing 20 mL acetone and 0.1 g treated diatom frustules was mixed with WCl_6 (0.13 g) and resol precursor (0.1 g, 20 wt% in THF) and vigorously stirred for 10 min. After adding 0.25 mL anhydrous ethanol, the suspension was sonicated for 2 h. The obtained mixture was concentrated on a heater at 50 °C for 8 h, and then dried at 100 °C for additional 8 h. The solid was calcined at 700 °C for 2 h under N_2 atmosphere. Finally, the as-synthesized nanohybrids were emerged in 10 wt% HF solution for 24 h to remove silica cores. Pure WO_3 nanorods were

synthesized using the same procedure without adding resol precursor and diatom cells to the solution.

2.3. Characterization

The phase purity and crystal structure of the materials were studied using a Bruker D8 (Germany) diffractometer with Cu radiation (Kα line with a mean wavelength of 1.54184 Å) operated at 40 kV. The morphologies were studied by a transmission electron microscope (TEM, JEM-2100F, JEOL, Japan) and a scanning electron microscope (SEM, Zeiss Sigma HD VP, Zeiss NTS, Cambridge, UK) equipped with an energy dispersive x-ray spectrometer (EDS, Thermo Pathfinder v1.4, Madison, WI, USA). The Raman spectroscopy was performed using a spectrometer (Ntegra Spectra NT-MDT, Russia) under a laser excitation at 532 nm. The textural characteristics of the samples were evaluated by conducting N_2 adsorption-desorption analysis at 77 K with Micromeritics 3Flex (USA) analyzer. Brunauer-Emmett-Teller (BET) and Barrett–Joyner–Halenda (BJH) methods were applied to measure total pore volume, surface area and pore size distribution. X-ray photoelectron spectroscopy (XPS) was conducted using a Escalab 250Xi Thermo Fisher Scientific XPS spectrometer (USA). ESR spectra were obtained on a Bruker ESR 300E electron paramagnetic resonance spectrometer to detect the active species using 5,5-dimethyl-1-pyrroline N-oxide (DMPO) as a spin-trapping agent.

2.4. Electrochemical and optical studies

The electrochemical measurements were conducted using a PGSTAT 128 N potentiostat–galvanostat (Metrohm Autolab, the Netherlands). To prepare working electrode, 40 mg of photocatalyst was mixed with a solution of ethanol (800 μL) and Nafion (5%, 200 μL) and dispersed using ultrasonication for 3 h. The resulted uniform suspension was dip-coated onto a 1 × 1 cm^2 glassy carbon electrode with a geometric area of 0.07 cm^2 followed by overnight

drying at ambient temperature. A saturated calomel electrode and platinum were applied as the reference and counter electrodes, respectively. LSV was performed at a scan rate of 10 mV s^{-1}. Electrochemical impedance spectra (EIS) were recorded at an overpotential of 200 mV vs normal hydrogen electrode (NHE) with an amplitude of 5.0 mV and a frequency range from 100 kHz to 0.01 Hz in Na_2SO_4 solution (0.5 M). Photoluminescence (PL) spectroscopy was performed using a Perkin Elmer LS45 (USA) spectrometer. Photoluminescence (PL) spectroscopy was performed using a Perkin Elmer LS45 (USA) spectrometer. To determine the E_g of the photocatalysts, ultraviolet-visible diffuse reflectance spectra (UV-Vis DRS) were collected using an S-250 Analytik Jena spectrophotometer (Germany).

2.5. Photocatalytic activity test for H_2 evolution

The photocatalytic H_2 evolution tests were carried out in 100 mL Pyrex flask at atmospheric pressure and room temperature. Typically, the photocatalyst sample (50 mg) was added into 80 mL of Na_2SO_3 (0.25 M) and Na_2S (0.35 M) solution followed by sonication for 60 min. Before starting the irradiation, the suspension was degassed by bubbling with highly pure N_2 gas for 0.5 h to ensure an anaerobic condition. A LED lamp ($\lambda > 420$ nm, 300 W, Shenzhen StarVanq Technology, China) was applied as the irradiation source. During the experiment, the suspension was mixed by a magnetic stirrer to keep the catalyst powder in suspension state. The generated H_2 was analyzed by a gas chromatography system (Agilent Technologies 7890A, TCD).

2.6. Photocatalytic activity test for CFZ degradation

CFZ was chosen as target emerging contaminant to examine the photocatalytic activities of the as-senthesized materials for treatment of antibiotic polluted water. Briefly, 60 mg of photocatalyst was dispersed into CFZ (100 mL, 3 mM) solution and the suspension was stirred

for 30 min under the dark condition to obtain adsorption-desorption equilibrium. Consequently, the light source was turned on and the suspension was exposed to visible irradiation using the same LED lamp mentioned in section 2.5. During photocatalysis, 2.0 mL of the treated CFZ solution was taken out at given time intervals followed by centrifugation for 5 min. The degradation of CFZ was determined by a high-performance liquid chromatography system (HPLC, HP-1090 Series II, USA), coupled with a C18 column and UV detector at 272 nm. The temperature of the column was adjusted at 45 °C. The mobile phase composed of 17% acetonitrile and 83% disodium hydrogen phosphate buffer was eluted at a flow-rate of 1.2 mL min^{-1}. The detection limit was estimated to be 2.8 μmol L^{-1} by plotting the calibration curves from 10 μM to 100 μM. Intermediates were detected using an Agilent 6890 gas chromatography (GC, Canada) instrument coupled to an Agilent 5973 mass spectrometer (MS, Canada) with a TG-5MS capillary column. More detailed description has been given elsewhere on the method used for preparation of the sample and the procedure of the identification of the intermediates (Khataee et al. 2017). TOC concentration was determined by a multi N/C 2100S TOC Analyzer. Anions concentrations were measured using an ion chromatography system (Dionex ICS-2100, USA).

3. Results and Discussion

3.1. Structural and morphological characteristics

The SEM image of the untreated diatom cell is shown in Fig. 1 (a). The *Cyclotella sp.* frustules are covered by some impurities and have a disk-like morphology with an outer diameter of ~7 μm. To remove these materials, the diatom frustules were treated using ultrasound-assisted H_2O_2/Fe^{2+} process. Fig. 1 (b) and (c) show that all the impurities and organic materials surrounding the cell walls are removed during treatment of *Cyclotella sp.* cells. The treated diatoms possess highly ordered nanoporous structure and the pores with controlled size

(diameter = 10-15 nm) are uniformly distributed on the cell walls. The SEM images of DT-WO_{3-x}@MC sample are displayed in Fig. 1 (d-f). As can be seen from Fig. 1 (d), the DT-WO_{3-x}@MC nanohybrid shows a similar morphology with nearly the same diameter of diatom template. It is observed that the surface of the diatom template is covered with WO_{3-x}@MC nanohybrid and the 3D morphology of the fabricated nanostructures maintain even after removing the template. The primary 3D architecture continues to grow in a homocentric growth style, and subsequently, the hierarchical nanostructures with a hole in the center can be formed during EISA process. Fig. 1 (e and f) exhibits that the entire hierarchical 3D nanostructures are decorated by homogeneously dispersed nanorods with an average diameter of ~20 nm. Fig. A1 (a-c) shows the EDS spectra of untreated frustule, treated frustule and DT-WO_{3-x}@MC samples, respectively. The presence of elements such as carbon, oxygen, silicon and calcium atoms can be observed in spectra of both untreated and treated frustules. However, the intensity of the carbon peak considerably decreases and the intensity of the peak ascribed to silicon remarkably increases after removing organic materials from the surface of frustule. This can be due to the purification of diatom frustule which is mainly composed of silica. Furthermore, the EDS spectrum of DT-WO_{3-x}@MC shows an intense peak assigned to tungsten beside carbon and oxygen peaks which reveals the successful synthesis of WO_{3-x}@MC nanohybrid using diatom template with no impurities (Gholami et al. 2020a).

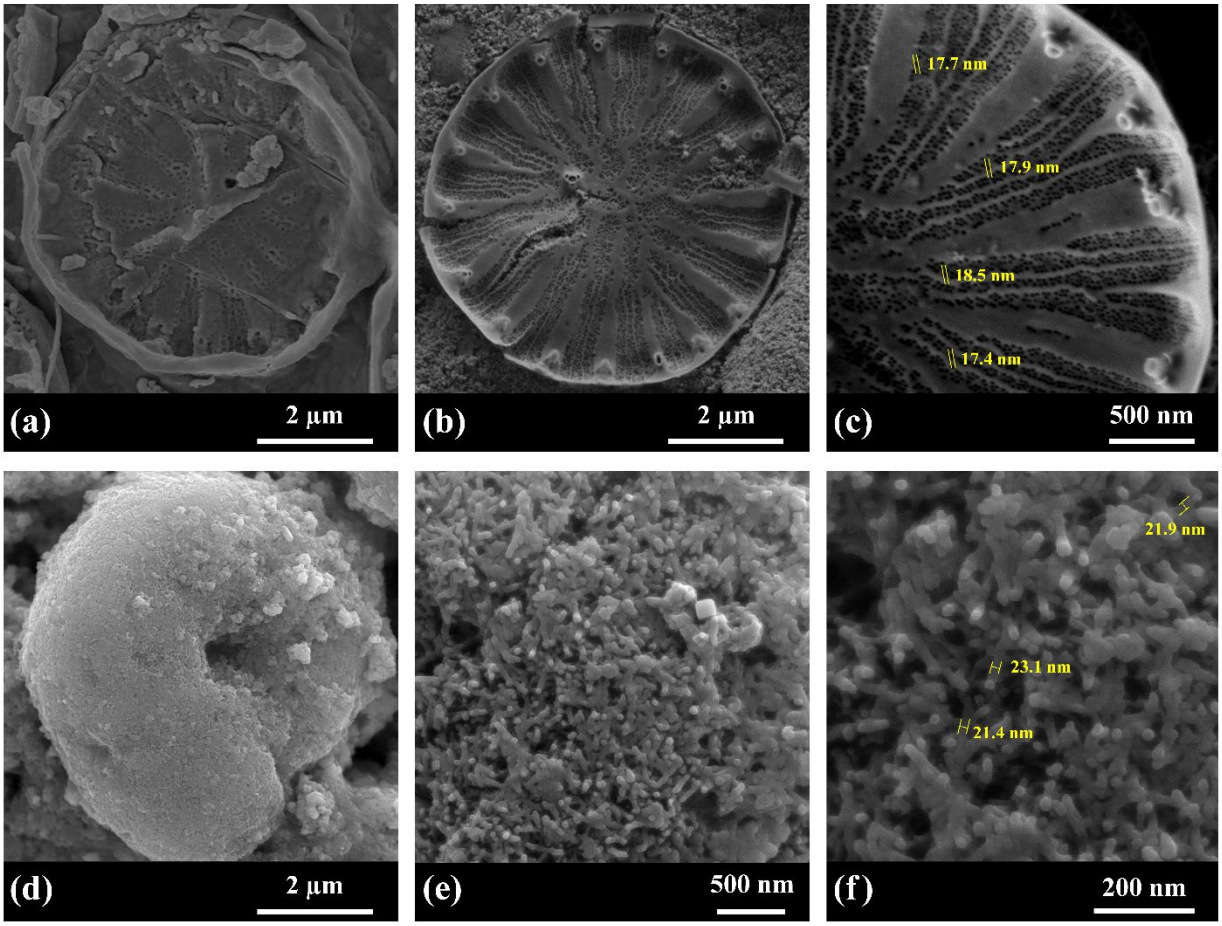

Fig. 1. SEM images of untreated frustule (a), treated frustule (b and c), and DT-WO_{3-x}@MC nanohybrid (d-f).

High-resolution TEM (HRTEM) analysis was performed to provide additional insights regarding morphological and structural properties of WO_3 nanorods and WO_{3-x}@MC nanohybrid. As can be seen from Fig. 2 (a and b), WO_3 nanorods with a diameter of ~20 nm and length of ~120 nm have a relatively uniform morphology. The interplaner distances of ~0.377 and ~0.373 nm between the regular lattice fringes can be corresponded to the (002) and (020) crystal planes of hexagonal tungsten trioxide [Fig. 2 (c)] (Chandra et al. 2019). TEM image of WO_{3-x}@MC nanohybrid [Fig. 2 (d)] reveals that tungsten oxide nanorods are entirely and homogeneously incorporated into mesoporous carbon structure. The representative HRTEM images [Fig. 2 (e and f)] demonstrate the interplanar spacing of ~0.383 nm, which

253 are related to (010) plane of $WO_{2.9}$, reveling the growth of the partially reduced tungsten
254 trioxide nanorods in the carbon matrix (Li et al. 2019b; Zhao et al. 2020).

255

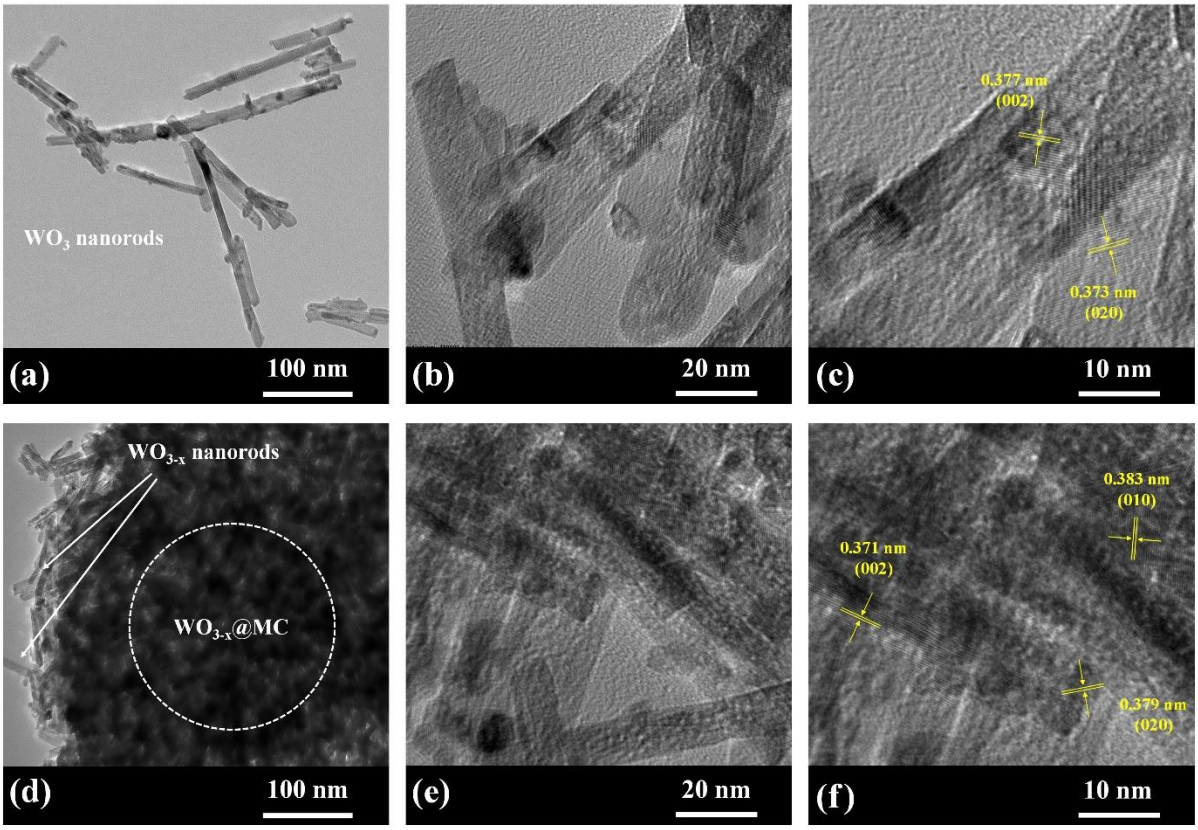

256

257 **Fig. 2.** TEM and HRTEM images of WO_3 nanorods (a-c) and DT-WO_{3-x}@MC nanohybrid (d-f).

258

259 Crystallinity and structural properties of the synthesized materials were studied via XRD
260 analysis. The XRD patterns of the diatom frustules, WO_3, and DT-WO_{3-x}@MC samples are
261 shown in Fig. 3 (a). XRD pattern diatom frustule displays no sharp diffraction, demonstrating
262 the amorphous feature of the sample. A wide peak expanded from 13.5° to 29.9° indicates the
263 existence of amorphous silica phase in diatom frustule (Shen & Zhang 2019). A similar pattern
264 has been reported in a large number of materials like diatoms (Nowak et al. 2019), opal-A (Sun
265 et al. 2018), and silica gel (Popkov et al. 2019) which contain amorphous silica. It can be

observed that the XRD pattern of pure WO_3 shows the diffraction peaks located at $2\theta = 13.7°$, 22.8°, 24.1°, 26.6°, 28.1°, 33.3°, 36.4°, 46.4°, and 57.2°, corresponding to the (100), (001), (110), (101), (200), (111), (201), (002), (301), and (311) planes of WO_3 (JCPDS No. 75-2187). The unit cell parameters for the pure WO_3 were calculated to be a = 7.281 Å and c = 3.903 Å, which are in good accordance with those of hexagonal tungsten trioxide (Tu et al. 2018). Compared with pure WO_3, the XRD pattern of DT-WO_{3-x}@MC sample contains a broad peak at ~25° and three extra diffraction peaks centered at 42.5°, 48.2°, and 54.9°. The peaks observed at ~25° and 42.5° can be attributed to the (002) and (100) plans of graphite phase (JCPDS No. 08-0415) revealing the formation of mesoporous carbon through addition of resol precursor to the reaction medium during synthesis of DT-WO_{3-x}@MC (Zhou et al. 2019). Meanwhile, the additional peaks located at 48.2° and 54.9° can be assigned to (220) and (310) plans of $WO_{2.9}$ (JCPDS No. 18-1417) which demonstrate the reducing role of carbon precursor during heat-treatment (Li et al. 2019c). The mean crystallite sizes of pure and MC modified tungsten oxide were calculated to be 24 and 18 nm, respectively, from the full width at half maximum (FWHM) of (200) plan using the Debye-Scherrer formula (Gu et al. 2019):

$$D_{XRD} = \frac{K\lambda}{\beta\cos\theta} \qquad (1)$$

where D_{XRD} is crystallite size in nm, β is the FWHM in radian, λ is the X-ray wavelength (1.5418 Å), K is the unitless Scherrer constant (0.89) and θ is the Bragg angle. These results show that the diatom surface can act as a nucleation agent for graphitization of carbon precursor and growth of tungsten oxide nanorods resulting in production of a nanostructured material with smaller crystallite size (Hu et al. 2017; de Moraes et al. 2020).

XPS spectroscopy was performed to investigate the elemental valence and surface electronic characteristics of the samples. Fig. 3 (b) displays the XPS spectra of the samples. Both WO_3 and DT-WO_{3-x}@MC display the existence of the same elements as confirmed from

the main peaks at 35.7, 284.8 and 533.7 eV in XPS full spectra attributing to W 4f, C 1s and O 1s, respectively. The elemental composition of WO_3 was determined to be C=15.3 at%, W=18.6 at% and O=66.1 at%. XPS composition of DT-WO_{3-x}@MC shows higher carbon content of 47.4 at% with W and O content of 14.9 at% and 37.7 at%, respectively. In comparison to the pure WO_3, the C1s peak on the DT-WO_{3-x}@MC spectrum is considerably intense, revealing the production of mesoporous carbon during synthesis of the nanohybrid material. The W 4f high-resolution spectrum of WO_3 exhibits two peaks at 35.6 and 37.7 eV, corresponding to 4f7/2 and 4f5/2, respectively, demonstrating that the main part of tungsten in the structure of WO_3 is in 6+ oxidation state [Fig. 3 (c)] (Zhan et al. 2019a). However, the W4f curve of DT-WO_{3-x}@MC shows new peaks at 34.3 and 36.6 eV which are ascribed to W^{5+}. These results are well in consistent with those achieved from XRD analysis and reveal that tungsten oxide is partially reduced by resol polymer during EISA process (Tu et al. 2018; Cui et al. 2019).

Raman spectroscopy provided more detailed structural and electronic characteristics of the samples [Fig. 3 (d)]. The peaks 713 and 806 cm^{-1} are assigned to the stretching modes of ν(O–W–O), while 272 and 323 cm^{-1} are attributed to the bending modes of δ(O–W–O) (Pervez et al. 2015; Yan et al. 2015). In addition, there are two broad bands located at 1351 and 1594 cm^{-1} in DT-WO_{3-x}@MC spectrum, respectively. The band at 1351 cm^{-1} (D-band) is attributed to the A_{1g} vibration of carbon and the band at 1594 cm^{-1} (G-band) is associated with the E_{2g} vibration of sp^2-bonded carbon (Pervez et al. 2015; Yan et al. 2015). These results are in good accordance with those reported by Pervez et al. for WO_3 mesosponge@Carbon (Pervez et al. 2015). Comparing the Raman spectrum of pure WO_3 with that of synthesized nanohybrid material confirms successful fabrication of WO_{3-x}@MC.

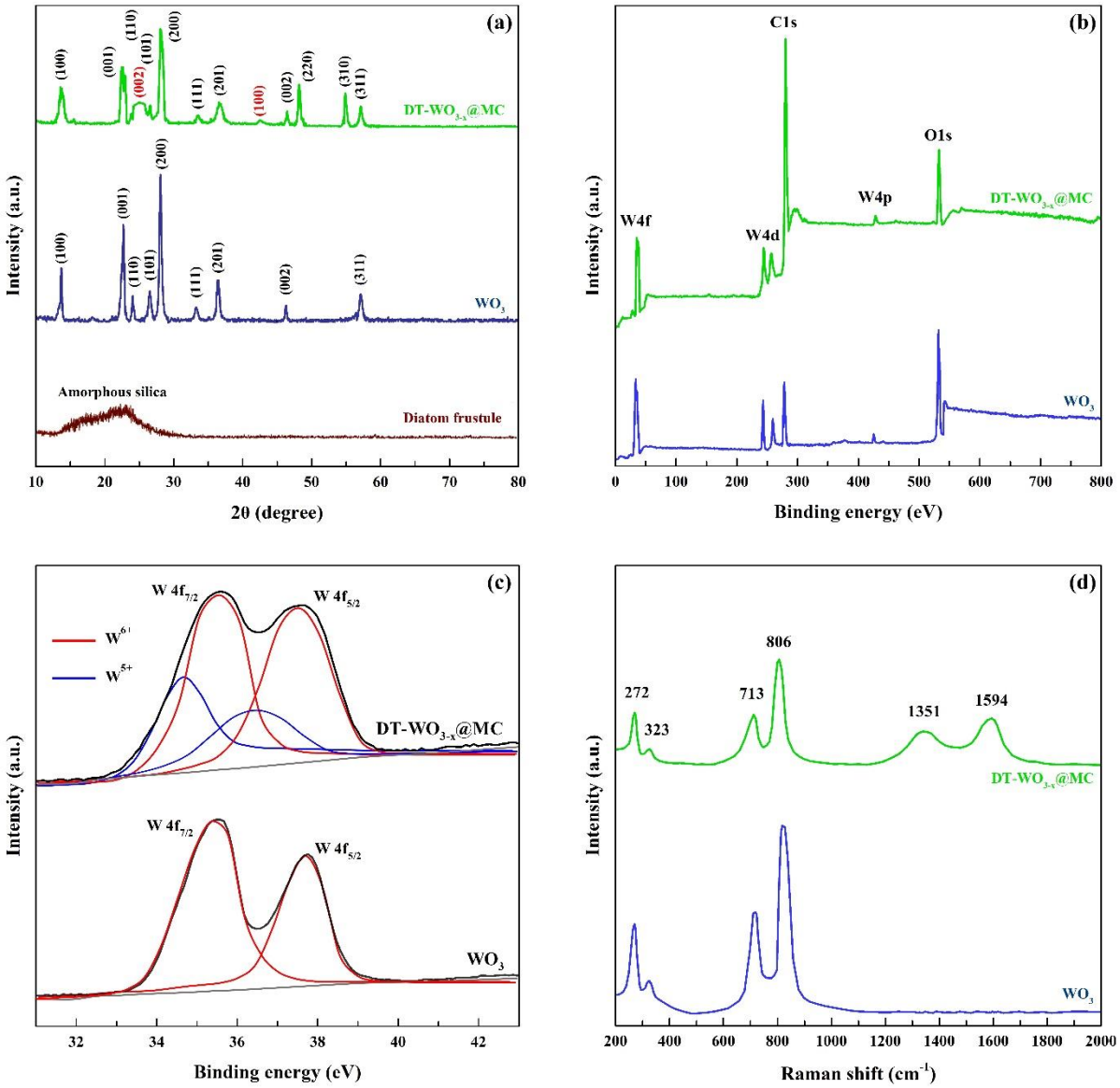

313

314 **Fig. 3.** XRD patterns (a), XPS full spectra (b), W 4f high-resolution spectra (c) and Raman

315 spectra, (d) of WO_3 nanorods and DT-WO_{3-x}@MC nanohybrid.

316

317 Fig. 4 (a) shows nitrogen adsorption-desorption isotherms of diatom frustules, WO_3 and

318 DT-WO_{3-x}@MC. All the developed materials show isotherms of type IV with a distinct type

319 H3 hysteresis loops according to the IUPAC classification, which is the property of

320 mesoporous materials [Fig. 4 (a)] (Su et al. 2016). The obtained results were analyzed by

321 Brunauer–Emmett–Teller (BET) and Barrett–Joyner–Halenda (BJH) methods to gain

information regarding specific surface area, total pore volume, and pore size distribution of the samples, respectively (Table A1). The pore size distribution peaks [Fig. 4 (b)] are well concentrated at 18.13, 11.42, 6.59 nm for diatom frustules, WO_3 and DT-WO_{3-x}@MC, respectively. The smaller S_{BET} and total pore volume of WO_3 are due to its high density. It is assumed that reduced WO_3 in DT-WO_{3-x}@MC nanohybrid possesses the density close to WO_3 density because it exhibits similar crystallinity and morphology as WO_3, based on the results obtained from XRD and HRTEM analyses. However, when WO_{3-x} is integrated with the MC, the S_{BET} and total pore volume enhance from 87.52 m^2 g^{-1} and 0.10 cm^3 g^{-1} to 195.37 m^2 g^{-1} and 0.393 cm^3 g^{-1}, respectively. This is due to the formation of highly ordered mesoporous nanostructures resulted from effective carbonization at a relatively high temperature, leaving a lot of void spaces within the carbon structure (Kong et al. 2019).

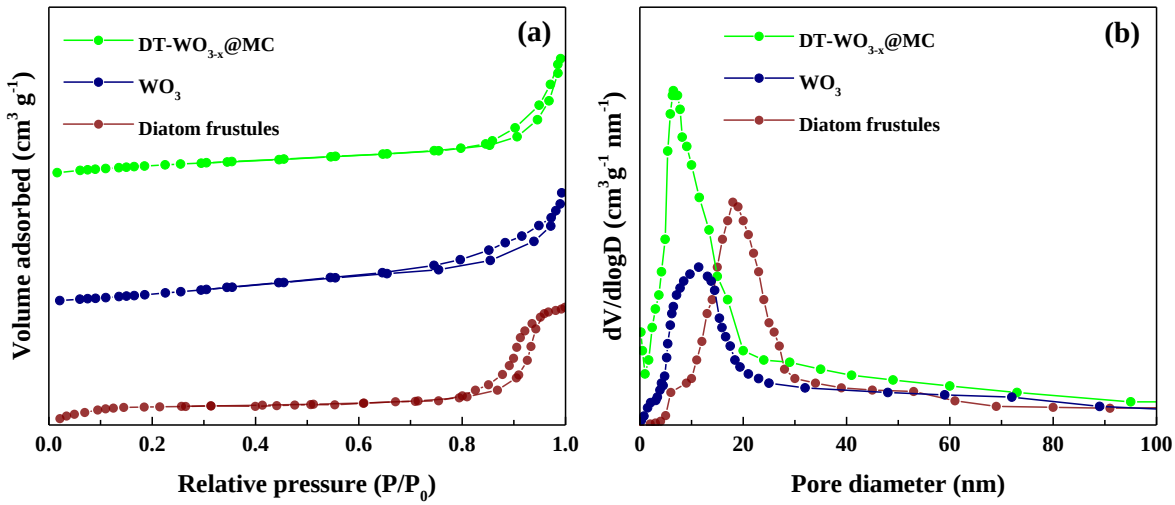

Fig. 4. N_2 adsorption-desorption isotherms (a) and pore size distributions (b) of diatom frustules, WO_3 and DT-WO_{3-x}@MC.

3.2. Optical and electrochemical properties

The UV–Vis DRS spectra were collected to evaluate the light absorption potential of the as-synthesized materials. It is obviously observed in Fig. 5 (a) that WO_3 has high absorption in the UV region with insignificant visible light harvesting. However, the DT-WO_{3-x}@MC shows a wide and intense absorption across both UV and visible regions, demonstrating the generation of further photo-produced electron-hole pairs under whole wavelength range, especially visible region. Therefore, the nanohybrid photocatalyst containing MC can efficiently harvest visible light to produce charge carriers. Moreover, the weak band at around 320 nm in absorption spectrum of DT-WO_{3-x}@MC can be attributed to the polycyclic aromatic hydrocarbons (π-conjugated species) which is consistent with previous works (Zhang et al. 2017).

The E_g of the WO_3 and DT-WO_{3-x}@MC were measured to be 2.85 and 2.67 eV as the slopes of curves of $(\alpha h\upsilon)^2$ versus $h\upsilon$, where h, υ, and α are Planck constant, light frequency and absorbance coefficient, respectively [Fig. 5 (b)] (Kumar et al. 2018). Integration of mesoporous carbon could increase the light absorption efficiency of the photocatalyst by two reasons. Firstly, the existence of mesoporous carbon can directly accelerate the separation of photo-produced carrier and improve electron delocalization in the system, thus enhancing the photocatalytic activity (Ding et al. 2018; Sun et al. 2019). Secondly, it is demonstrated using XRD and XPS analyses that WO_3 is partially reduced to WO_{3-x} by resol polymer during EISA synthesis; the presence of oxygen vacancies can produce filled impurity bands that considerably decrease the E_g (Wang et al. 2018).

The PL spectroscopy is a useful analysis to investigate surface photochemical processes involving photo-excited charge carriers from semiconductor materials. As illustrated in Fig. 5 (c), the PL intensity resulted from DT-WO_{3-x}@MC is lower than that of pure WO_3 nanorods, indicating more effective prevention of electron-hole pairs recombination in the nanohybrid photocatalyst. This is ascribed to the incorporation of high-conductive mesoporous carbon in 3D structure of DT-WO_{3-x}@MC which could act as an electron acceptor to receive and shuttle

the electrons generated from WO_3 through light excitation (Zhan et al. 2019b). As a consequent, the separation and lifetime of charge carriers are enhanced, resulting in the improved photocatalytic performance of the DT-WO_{3-x}@MC nanohybrid.

The electron-transport capacity of the samples was studied by electrochemical impedance spectroscopy (EIS) test [Fig. 5 (d)]. Generally, in order to determine the variations in the interfacial characteristics, the changes in the electrochemical impedance are essential indicators. In semiconductors, a high interfacial transport facilitates the separation of the charge carriers and weakens the recombination phenomenon, and this results in reduced impedance. The arc radius of the EIS Nyquist plot of the DT-WO_{3-x}@MC nanohybrid is smaller than that of pure tungsten oxide, revealing a quicker interfacial charge transport to the electron acceptor, which leads to the effective electron-hole pairs separation (Zhang et al. 2017). In fact, following the excitation of photoproduced electrons from the valence band (VB) to the conduction band (CB) of WO_{3-x}, they are then transported to mesoporous carbon, preventing the fast recombination of electron-hole pairs. The MC is a good electron acceptor due to its conjugated structure, which makes it a separation center for the excited electrons and holes (Yang et al. 2017a). Zhang et al. have also reported a red-shift of the band edge absorption for WO_{3-x}/C compared to pure WO_3 and demonstrated that carbon coating and oxygen vacancies bring WO_{3-x}/C strong absorption at higher wavelengths and improve the charge carrier separation performance (Zhang et al. 2020b).

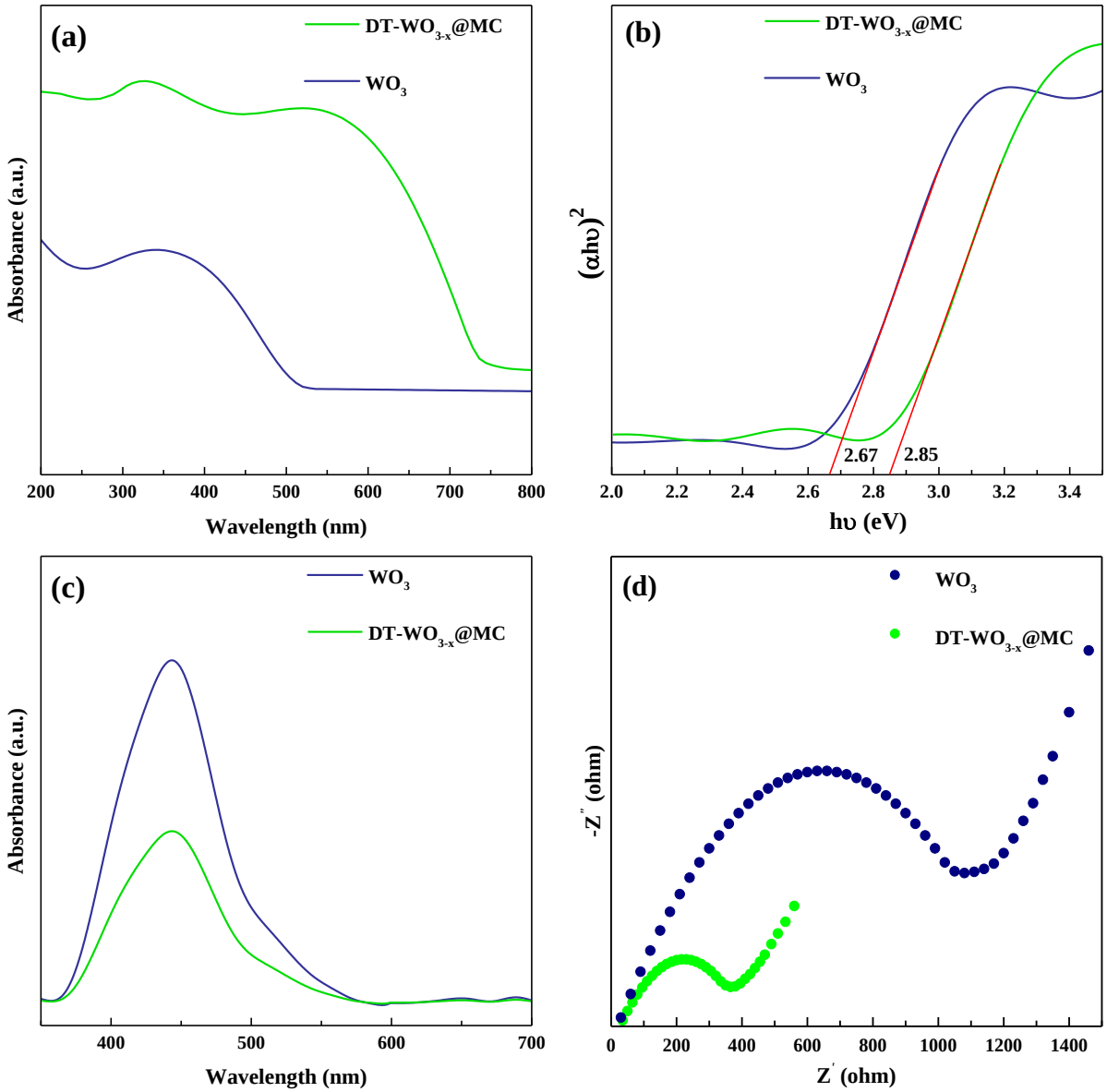

Fig. 5. UV-DRS (a), $(\alpha h\upsilon)^2$-hυ plots (b), PL spectra (c) and EIS Nyquist plots (d) of WO_3 nanorods and DT-WO_{3-x}@MC nanohybrid.

3.3. Photocatalytic H_2 production

Fig. 6 (a) represents the photocatalytic H_2 evolution from water using WO_3 and DT-WO_{3-x}@MC photocatalysts under visible light irradiation. When the light is irradiated on the photocatalyst surface, the electrons and holes are formed at the photocatalyst/solution interface according to Eq. (2), and take part in reduction and oxidation processes, respectively

(Gomathisankar et al. 2013). The holes convert water molecules to H^+ ions and $^{\bullet}OH$ radicals [Eq. (3)] . At the same time, the electrons react with H_2O and H^+ to produce hydrogen molecules [Eq. (4) and (5), respectively]. Na_2S/Na_2SO_3 is used as sacrificial reagents to scavenge the generated holes based on Eqs. (6-9). The generation of S_2^{2-} anions, which act as optical filters and compete with proton reduction, is inhibited by adding SO_3^{2-} anions resulting in production of thiosulfate anions (Gomathisankar et al. 2013).

$$DT-WO_{3-x}@MC + h\upsilon \rightarrow DT-WO_{3-x}@MC(h^+ + e^-) \quad (2)$$

$$H_2O + h_{VB}^+ \rightarrow {}^{\bullet}OH + H^+ \quad (3)$$

$$2H_2O + 2e_{CB}^- \rightarrow H_2 + 2OH^- \quad (4)$$

$$2H^+ + 2e_{CB}^- \rightarrow H_2 \quad (5)$$

$$SO_3^{2-} + H_2O + 2h_{VB}^+ \rightarrow SO_4^{2-} + 2H^+ \quad (6)$$

$$2S^{2-} + 2h_{VB}^+ \rightarrow S_2^{2-} \quad (7)$$

$$S_2^{2-} + SO_3^{2-} \rightarrow S_2O_3^{2-} + S^{2-} \quad (8)$$

$$SO_3^{2-} + S^{2-} + 2h_{VB}^+ \rightarrow S_2O_3^{2-} \quad (9)$$

As can be seen in Fig. 6 (a), the relatively low H_2 production rate (746 μmol g^{-1} h^{-1}) is observed using WO_3 nanorods due to poor absorption in the visible region, large E_g, low specific surface area and limited charge transport. The 3D WO_{3-x}@MC nanohybrid shows almost 2.5 times higher photocatalytic efficiency (1851 μmol g^{-1} h^{-1}) than the WO_3 nanorods mainly owing to the improved light absorption, lower recombination of electrons and holes, higher specific surface area and higher electron transfer ability. The synthesized nanohybrid material in this study possesses higher photocatalytic H_2 production rate than previously reported WO_3-based photocatalysts (Zhang et al. 2019; Sun et al. 2020; Zhang et al. 2020c). In

DT-WO_{3-x}@MC system, initially, WO_{3-x} nanorods are excited to produce charge carriers under visible light irradiation. Subsequently, the photo-produced electrons in the CB of WO_{3-x} can be directly transported to MC via solid-solid interface because of its high electron transport ability and participate in the surface reduction for hydrogen production (Kailasam et al. 2015). On the other hand, the enhanced photocatalytic activity of synthesized nanohybrid should also be ascribed to its 3D structural advantages which can considerably decrease the diffusion length of charge migration and facilitate electron transfer on the surface terminal sites (Wan et al. 2018).

Fig. A2 represents the LSV curves of the photocatalysts. DT-WO_{3-x}@MC shows higher current density than WO_{3-x} nanorods indicating stronger electron migration. The LSV curve of a commercial Pt/C electrode was also evaluated, for comparison. The potential value for the current density of 10 mA cm^{-2} is a frequently used criterion to examine the electrochemical properties of photocatalysts (Zhao et al. 2016). Pt/C electrode exhibits extremely high activity with a very low overpotential (0.08 V vs NHE). The overpotential of DT-WO_{3-x}@MC at 10 mA cm^{-2} is found to be 0.13 V vs NHE which is smaller than that of WO_3 (2.9 vs NHE) and much closer to that of Pt/C electrode. The cycled photocatalytic runs were conducted to verify the stability of WO_3 nanorods and DT-WO_{3-x}@MC nanohybrid during long-term application as photocatalysts for H_2 production [Fig. 6 (b)]. The photocatalytic efficiencies of both synthesized materials exhibit no remarkable decrease during five repeated cycles for 20 h, confirming their high stability for visible-light-driven hydrogen production.

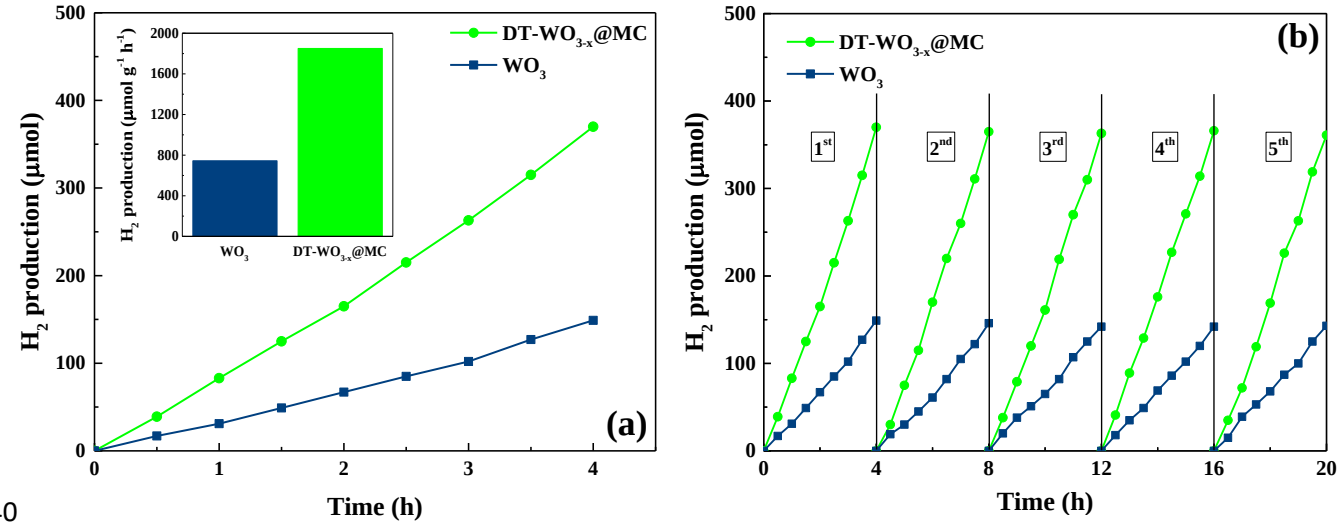

Fig. 6. Time course of hydrogen production and corresponding rate comparison (a) and cyclic stability (b) for WO_3 nanorods and DT-WO_{3-x}@MC nanohybrid under visible light; Experimental conditions: [photocatalyst] = 0.625 g L^{-1} and temperature = 30±1 °C.

3.4. Photocatalytic CFZ degradation

3.4.1. Comparison of WO_3 and DT-WO_{3-x}@MC

In order to further investigate the photocatalytic application of DT-WO_{3-x}@MC, a series of degradation experiments were done using CFZ as the target emerging contaminant. Control tests were carried out in the presence of catalysts and in the dark condition and it was found that the adsorption of CFZ on WO_3 and DT-WO_{3-x}@MC photocatalysts was negligible (9.4% and 13.1%, respectively). According to the obtained results, the role of visible light irradiation alone in the removal of CFZ is also inconsiderable (4.9%) within 90 min [Fig. 7 (a)]. The pure WO_3 displays a CFZ degradation efficiency of 35.4% within 90 min photocatalysis under visible-light irradiation. It has already been proved that WO_3 is an excellent photocatalyst for the degradation of different organic pollutants under UV light irradiation (Khan et al. 2018). However, the poor absorption, relatively wide band gap and fast recombination of electrons

and holes generated through Eq. (2), restrict the application of pure WO_3 in photo-degradation of different contaminants under visible light irradiation. Interestingly, the integration of MC and WO_{3-x} fabricates an superior nanohybrid photocatalyst which leads to the almost complete degradation of CFZ (98.7%) under the same operational conditions according to the following equations (Darvishi Cheshmeh Soltani et al. 2016):

$$DT - WO_{3-x}@MC(e_{CB}^{-}) + O_2 \rightarrow DT - WO_{3-x}@MC + O_2^{\bullet -} \qquad (10)$$

$$DT - WO_{3-x}@MC(h_{VB}^{+}) + H_2O \rightarrow DT - WO_{3-x}@MC + H^{+} + {}^{\bullet}OH \qquad (11)$$

When WO_{3-x} nanorods are uniformly embedded in 3D mesoporous carbon framework, further active sites are exposed to produce more oxidizing species and improve the CFZ degradation efficiency because of higher specific surface area. Furthermore, according to the results obtained from UV-Vis DRS, DT-WO_{3-x}@MC shows the enhanced absorption potential in the visible region compared to the WO_3 nanorods. Corresponding band gap measurement also revealed that E_g of DT-WO_{3-x}@MC (2.67 eV) is considerably lower than that of WO_3 nanorods (2.85 eV). In addition, integration of MC with WO_{3-x} as 3D structure developed by diatom template reduces the charge carriers recombination and increases the electron-transport capacity of the photocatalyst. The removal rate of CFZ by the studied systems was also investigated using pseudo-first order model [Eq. (12)] and the calculated values of rate constants (min^{-1}) were presented in Fig. 7 (b). As can be observed, the highest rate constant corresponds to the implementation of DT-WO_{3-x}@MC for degradation of CFZ. The apparent rate constant (k_{app}) value for the use of WO_3 under visible light irradiation is 62×10^{-4} min^{-1}, while the application of DT-WO_{3-x}@MC as photocatalyst results in the k_{app} value of 435×10^{-4} min^{-1}. To demonstrate the enhancement in photocatalytic degradation made by replacing WO_3 nanorods with DT-WO_{3-x}@MC nanohybrid, the synergy factors were determined using the

calculated k_{app} values for both WO_3 and DT-WO_{3-x}@MC based on Eqs. (13 and 14) as 3.6 and 18.9 (Gholami et al. 2019). The reusability of the nanohybrid was also studied by performing five successive runs. After each run, the photocatalyst was washed with distilled water and dried at room temperature. Then, a fresh pollutant solution was prepared and the next run was carried out under the identical operational conditions. As shown in Fig. A3, there is no considerable decrease in the photocatalytic activity of DT-WO_{3-x}@MC after 5 runs.

$$\ln(\frac{C_0}{C_t}) = k_{app}t \qquad (12)$$

$$Synergy \quad factor_{Vis/WO_3} = \frac{k_{app(Vis/WO_3)}}{k_{app(Vis)} + k_{app(WO_3)}} \qquad (13)$$

$$Synergy \quad factor_{Vis/DT-WO_{3-x}@MC} = \frac{k_{app(Vis/DT-WO_{3-x}@MC)}}{k_{app(Vis)} + k_{app(DT-WO_{3-x}@MC)}} \qquad (14)$$

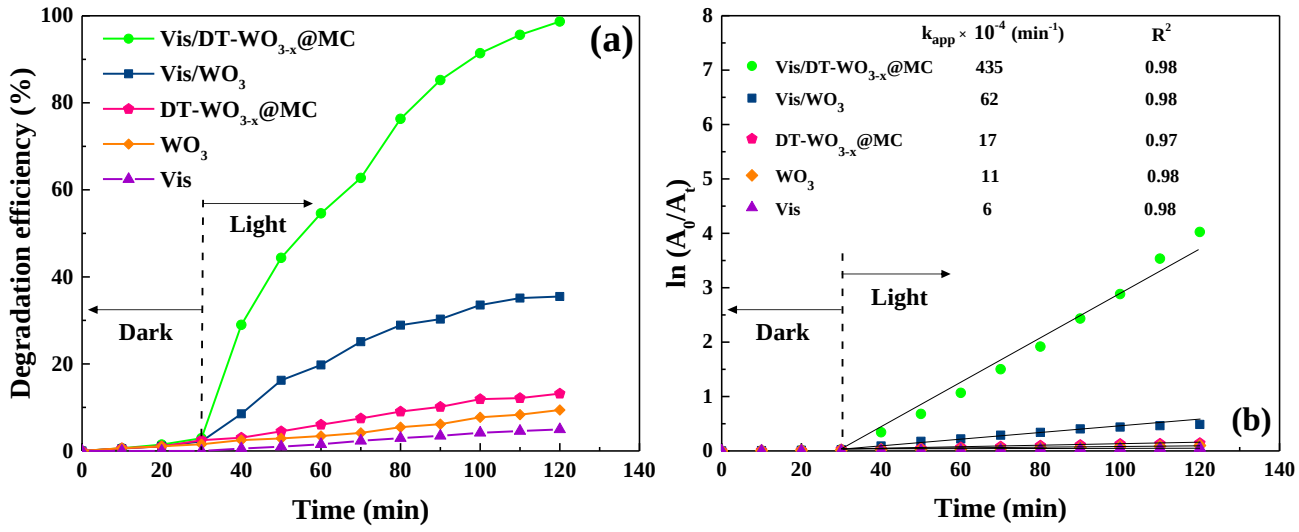

Fig. 7. Removal of CFZ using different processes (a) and corresponding kinetic analysis based on the pseudo-first-order model (b); Experimental conditions: [photocatalyst] = 0.6 g L^{-1}, [CFZ] = 3 mM, pH = 6.3 and temperature = 30±1 °C.

3.4.2. CFZ degradation mechanism and pathway

To detect the major reactive species involved in photocatalytic degradation of CFZ, scavenging experiments were carried out during photocatalysis using isopropanol (IPA), 1,4-benzoquinone (BQ), and ethylenediaminetetraacetic acid disodium salt (EDTA-2Na) as $^{\bullet}OH$, $O_2^{\bullet-}$ and h^+, scavengers, respectively (Kumar et al. 2018). The scavengers can inhibit the activity of oxidizing species, leading to the limited degradation of the pollutant molecules. The influence of scavenging species on photocatalytic degradation of CFZ is shown in Fig. 8 (a). All the scavenging species negatively affect the DT-WO_{3-x}@MC catalyzed CFZ photodegradation. EDTA-2Na (2 mM) has the lowest scavenging effect on the photocatalytic performance of DT-WO_{3-x}@MC, which indicates that h^+ may not play the main role in the degradation of CFZ. According to Eq. (15), $^{\bullet}OH$ radicals are mainly scavenged by the IPA molecules, generating isopropanol radicals (Wojnárovits et al. 2006). On the other hand, BQ can react with $O_2^{\bullet-}$ to produce semiquinone radicals based on Eq. (16) (Schneider et al. 2020). The addition of BQ led to a higher inhibiting effect than that of IPA, which reveals that $O_2^{\bullet-}$ acts as the most significant oxidizing species during photocatalysis. In the presence of 2 mM EDTA-2Na, IPA and BQ, the degradation efficiency decreases from 98.7% to 79.5%, 66.9% and 35.7%, respectively. ESR spin trapping technique was also applied to validate the observations for production of reactive oxygen species. As can be observed from Fig. 8 (b), the intensities of ESR signals of DMPO–$O_2^{\bullet-}$ are higher than those of DMPO–$^{\bullet}OH$ which further clarifies the key role of $O_2^{\bullet-}$ radicals during photodegradation of CFZ.

$$^{\bullet}OH + (CH_3)_2CHOH \rightarrow H_2O + (CH_3)_2C^{\bullet}OH \qquad (15)$$

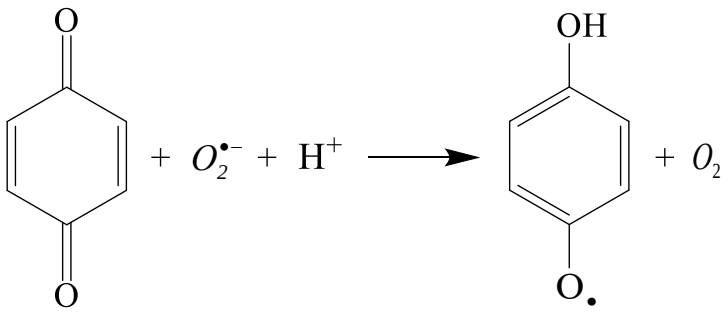

(16)

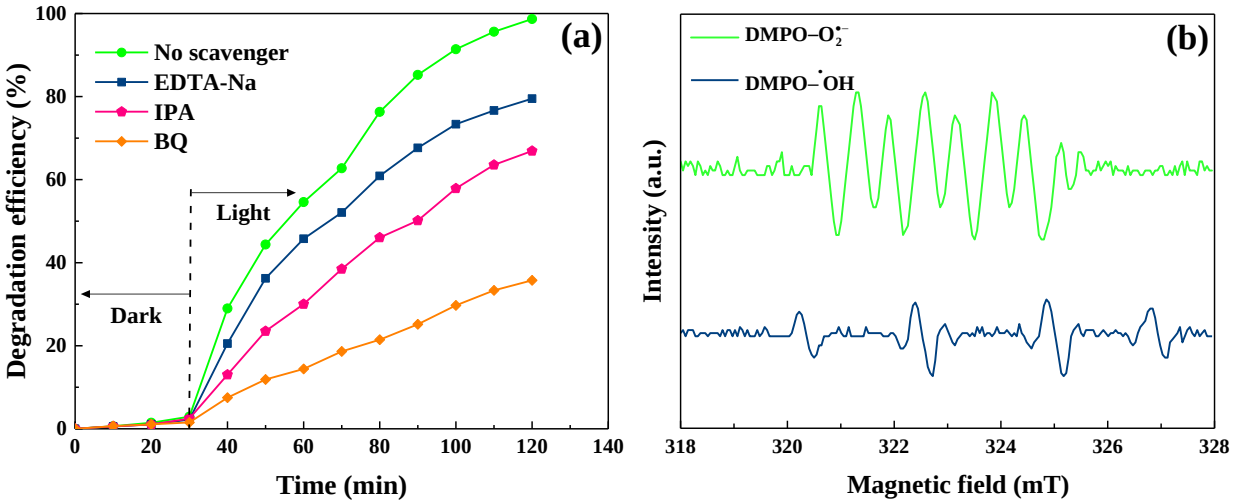

Fig. 8. (a) Effect of different scavengers on the CFZ degradation (Experimental conditions: [photocatalyst] = 0.6 g L^{-1}, [CFZ] = 3 mM, pH = 6.3, [scavenger] = 10 mM and temperature = 30±1 °C and (b) ESR spectra of DMPO–$O_2^{\bullet-}$ and DMPO–$^{\bullet}$OH.

The GC-MS was used to recognize the intermediates generated during the CFZ photodegradation. GC-MS spectra of detected intermediate compounds are shown in Fig. A4. Based on the identified by-products, three main competing pathways were suggested for the decomposition of CFZ (Fig. A5). In pathway I, the CFZ molecule is decomposed to 5-methyl-3H-1,3,4-thiadiazole-2-thiol. The –SH functional group is removed from 5-methyl-3H-1,3,4-thiadiazole-2-thiol and subsequently thiadiazole ring is broken to form 1-(hydroxymethyl)-3-

methylthiourea. In pathway II, the parent molecule is converted to 7-amino-3-methyl-8-oxo-5-thia-1-azabicyclo[4.2.0]oct-2-ene-2-carboxylic acid. Then, oxidation of β-lactam ring by reactive species precedes ring opening to generate aliphatic compounds like 2-methylbutanedioic acid and 2,3-diaminopropanoic acid. In pathway III, 2-(tetrazol-1-yl) acetic acid is firstly formed by the attack of reactive species. Subsequently, 2-(tetrazol-1-yl) acetic acid is decomposed to 2H-tetrazole and oxalic acid. For all the pathways, the as-generated compounds are finally oxidized to water, carbon dioxide and inorganic products. The TOC and IC analyses were performed to examine the ability of DT-WO_{3-x}@MC photocatalyst in mineralization of CFZ solution. The results obtained from TOC analysis demonstrates the TOC removal efficiencies of 61.2% and 83.5% within 90 and 180 min, respectively. Moreover, according to the results of IC analysis, the concentrations of NO_3^-, NH_4^+ and SO_4^{2-} increase from 0.47, 0.13 and 0.39 mg L^{-1} to 4.24, 1.93 and 1.37 mg L^{-1} after 90 min reaction time. This reveals the production of ionic products from the CFZ degradation. Reduction of TOC concentration as well as the release of sulfur and nitrogen species during the degradation process indicates the effective mineralization of CFZ solution.

4. Conclusions

In this work, *Cyclotella sp.* was utilized as a natural template to fabricate a highly ordered mesoporous carbon embedding reduced tungsten oxide nanorods through a one-pot evaporation-induced self-assembly method. The XRD and XPS analyses proved the successful synthesis of WO_3 nanorods and DT-WO_{3-x}@MC nanohybrid and partial reduction of tungsten oxide by resol precursor. The unique structure of diatom frustule could increase the specific surface area and available active sites of DT-WO_{3-x}@MC by avoiding aggregation. The results of EIS and PL analyses indicated that the recombination of electron-hole pairs was significantly

prevented by integrating reduced tungsten oxide and mesoporous carbon. The band gap value was calculated to be 2.85 and 2.67 eV for DT-WO_{3-x}@MC nanohybrid and WO_3 nanorods, respectively. DT-WO_{3-x}@MC exhibited a higher hydrogen production rate of 1851 μmol g^{-1} h^{-1} which was almost 2.5 times higher than that of WO_3 nanorods (746 μmol g^{-1} h^{-1}). Moreover, the rate constant of pseudo-first order model for photodegradation of CFZ using WO_3 and DT-WO_{3-x}@MC was calculated as 62×10^{-4} and 435×10^{-4} min^{-1}, respectively. $O_2^{\bullet-}$ radicals were found to be the most reactive species involved in degradation of CFZ by performing scavenging experiments and ESR analysis. The synthesized photocatalyst could be advantageous for degradation of target antibiotic pollutant, as EISA method for fabrication of DT-WO_{3-x}@MC involves a simple one-pot synthetic strategy using inexpensive diatom frustule as a natural template.

Acknowledgements

The authors wish to thank the University of Tabriz and University of Eastern Finland for their support. P. Gholami also gratefully acknowledges Centre for International Mobility (CIMO), Finland for providing EDUFI fellowship (decision number TM-18-10895).

References

Acharya, L., Nayak, S., Pattnaik, S.P., Acharya, R., Parida, K., 2020. Resurrection of boron nitride in p-n type-II boron nitride/B-doped-g-C_3N_4 nanocomposite during solid-state Z-scheme charge transfer path for the degradation of tetracycline hydrochloride. Journal of Colloid and Interface Science 566, 211-223

577 Cai, Z., Hao, X., Sun, X., Du, P., Liu, W., Fu, J., 2019. Highly active WO_3@anatase-SiO_2
578 aerogel for solar-light-driven phenanthrene degradation: Mechanism insight and
579 toxicity assessment. Water Research 162, 369-382.
580 Cha-Umpong, W., Hosseini, E., Razmjou, A., Zakertabrizi, M., Korayem, A.H., Chen, V.,
581 2020. New molecular understanding of hydrated ion trapping mechanism during
582 thermally-driven desalination by pervaporation using GO membrane. Journal of
583 Membrane Science 598, 117687.
584 Chandra, D., Li, D., Sato, T., Tanahashi, Y., Togashi, T., Ishizaki, M., Kurihara, M., Mohamed,
585 E.A., Tsubonouchi, Y., Zahran, Z.N., Saito, K., Yui, T., Yagi, M., 2019.
586 Characterization and mechanism of efficient visible-light-driven water oxidation on an
587 in situ N_2-intercalated WO_3 nanorod photoanode. ACS Sustainable Chemistry &
588 Engineering 7, 17896-17906.
589 Chen, D., Li, B., Pu, Q., Chen, X., Wen, G., Li, Z., 2019. Preparation of Ag-$AgVO_3$/g-C_3N_4
590 composite photo-catalyst and degradation characteristics of antibiotics. Journal of
591 Hazardous Materials 373, 303-312.
592 Cui, Y., Xiao, K., Bedford, N.M., Lu, X., Yun, J., Amal, R., Wang, D.-W., 2019. Refilling
593 nitrogen to oxygen vacancies in ultrafine tungsten oxide clusters for superior lithium
594 storage. Advanced Energy Materials 9, 1902148.
595 Darvishi Cheshmeh Soltani, R., Khataee, A., Mashayekhi, M., 2016. Photocatalytic
596 degradation of a textile dye in aqueous phase over ZnO nanoparticles embedded in
597 biosilica nanobiostructure. Desalination and Water Treatment 57, 13494-13504.
598 de Moraes, N.P., Valim, R.B., da Silva Rocha, R., da Silva, M.L.C.P., Campos, T.M.B., Thim,
599 G.P., Rodrigues, L.A., 2020. Effect of synthesis medium on structural and
600 photocatalytic properties of ZnO/carbon xerogel composites for solar and visible light

601 degradation of 4-chlorophenol and bisphenol A. Colloids and Surfaces A:
602 Physicochemical and Engineering Aspects 584, 124034.
603 Ding, N., Zhang, L., Hashimoto, M., Iwasaki, K., Chikamori, N., Nakata, K., Xu, Y., Shi, J.,
604 Wu, H., Luo, Y., Li, D., Fujishima, A., Meng, Q., 2018. Enhanced photocatalytic
605 activity of mesoporous carbon/C_3N_4 composite photocatalysts. Journal of Colloid and
606 Interface Science 512, 474-479.
607 Dong, S., Cui, L., Zhang, W., Xia, L., Zhou, S., Russell, C.K., Fan, M., Feng, J., Sun, J., 2020.
608 Double-shelled $ZnSnO_3$ hollow cubes for efficient photocatalytic degradation of
609 antibiotic wastewater. Chemical Engineering Journal 384, 123279.
610 Gholami, P., Dinpazhoh, L., Khataee, A., Orooji, Y., 2019. Sonocatalytic activity of biochar-
611 supported ZnO nanorods in degradation of gemifloxacin: Synergy study, effect of
612 parameters and phytotoxicity evaluation. Ultrasonics Sonochemistry 55, 44-56.
613 Gholami, P., Khataee, A., Bhatnagar, A., 2020a. Environmentally superior cleaning of diatom
614 frustules using sono-Fenton process: Facile fabrication of nanoporous silica with
615 homogeneous morphology and controlled size. Ultrasonics Sonochemistry 64, 105044.
616 Gholami, P., Khataee, A., Soltani, R.D.C., Dinpazhoh, L., Bhatnagar, A., 2020b. Photocatalytic
617 degradation of gemifloxacin antibiotic using Zn-Co-LDH@biochar nanocomposite.
618 Journal of Hazardous Materials 382, 121070.
619 Gomathisankar, P., Hachisuka, K., Katsumata, H., Suzuki, T., Funasaka, K., Kaneco, S., 2013.
620 Photocatalytic hydrogen production from aqueous Na_2S + Na_2SO_3 solution with B-
621 doped ZnO. ACS Sustainable Chemistry & Engineering 1, 982-988.
622 Gora, S.L., Andrews, S.A., 2019. Removal of natural organic matter and disinfection byproduct
623 precursors from drinking water using photocatalytically regenerable nanoscale
624 adsorbents. Chemosphere 218, 52-63.

Gu, F., Cui, Y., Han, D., Hong, S., Flytzani-Stephanopoulos, M., Wang, Z., 2019. Atomically dispersed Pt (II) on WO_3 for highly selective sensing and catalytic oxidation of triethylamine. Applied Catalysis B: Environmental 256, 117809.

Guo, M., Xing, Z., Zhao, T., Li, Z., Yang, S., Zhou, W., 2019. WS_2 quantum dots/MoS_2@WO_{3-x} core-shell hierarchical dual Z-scheme tandem heterojunctions with wide-spectrum response and enhanced photocatalytic performance. Applied Catalysis B: Environmental 257, 117913.

Hu, K., Li, R., Ye, C., Wang, A., Wei, W., Hu, D., Qiu, R., Yan, K., 2020b. Facile synthesis of Z-scheme composite of TiO_2 nanorod/g-C_3N_4 nanosheet efficient for photocatalytic degradation of ciprofloxacin. Journal of Cleaner Production 253, 120055.

Hu, P., Long, M., Bai, X., Wang, C., Cai, C., Fu, J., Zhou, B., Zhou, Y., 2017. Monolithic cobalt-doped carbon aerogel for efficient catalytic activation of peroxymonosulfate in water. Journal of Hazardous Materials 332, 195-204.

Jamila, G.S., Sajjad, S., Leghari, S.A.K., Long, M., 2020. Nitrogen doped carbon quantum dots and GO modified WO_3 nanosheets combination as an effective visible photo catalyst. Journal of Hazardous Materials 382, 121087.

Kailasam, K., Fischer, A., Zhang, G., Zhang, J., Schwarze, M., Schröder, M., Wang, X., Schomäcker, R., Thomas, A., 2015. Mesoporous carbon nitride-tungsten oxide composites for enhanced photocatalytic hydrogen evolution. ChemSusChem 8, 1404-1410.

Khan, H., Rigamonti, M.G., Patience, G.S., Boffito, D.C., 2018. Spray dried TiO_2/WO_3 heterostructure for photocatalytic applications with residual activity in the dark. Applied Catalysis B: Environmental 226, 311-323.

Khataee, A., Kayan, B., Gholami, P., Kalderis, D., Akay, S., Dinpazhoh, L., 2017. Sonocatalytic degradation of Reactive Yellow 39 using synthesized ZrO_2 nanoparticles on biochar. Ultrasonics Sonochemistry 39, 540-549.

Kobya, M., Soltani, R.D.C., Omwene, P.I., Khataee, A., 2020. A review on decontamination of arsenic-contained water by electrocoagulation: Reactor configurations and operating cost along with removal mechanisms. Environmental Technology & Innovation 17, 100519.

Kong, N., Jia, M., Yang, C., Lan, J., Yu, Y., Yang, X., 2019. Encapsulating V_2O_3 nanoparticles in carbon nanofibers with internal void spaces for a self-supported anode material in superior lithium-ion capacitors. ACS Sustainable Chemistry & Engineering 7, 19483-19495.

Kumar, A., Rana, A., Sharma, G., Naushad, M., Al-Muhtaseb, A.a.H., Guo, C., Iglesias-Juez, A., Stadler, F.J., 2018. High-performance photocatalytic hydrogen production and degradation of levofloxacin by wide spectrum-responsive Ag/Fe_3O_4 bridged $SrTiO_3$/g-C_3N_4 plasmonic nanojunctions: Joint effect of Ag and Fe_3O_4. ACS Applied Materials & Interfaces 10, 40474-40490.

Lee, C.-G., Javed, H., Zhang, D., Kim, J.-H., Westerhoff, P., Li, Q., Alvarez, P.J.J., 2018. Porous electrospun fibers embedding TiO_2 for adsorption and photocatalytic degradation of water pollutants. Environmental Science & Technology 52, 4285-4293.

Li, B., Lai, C., Zeng, G., Qin, L., Yi, H., Huang, D., Zhou, C., Liu, X., Cheng, M., Xu, P., Zhang, C., Huang, F., Liu, S., 2018a. Facile hydrothermal synthesis of Z-scheme $Bi_2Fe_4O_9/Bi_2WO_6$ heterojunction photocatalyst with enhanced visible light photocatalytic activity. ACS Applied Materials & Interfaces 10, 18824-18836.

Li, K., Liu, X., Zheng, T., Jiang, D., Zhou, Z., Liu, C., Zhang, X., Zhang, Y., Losic, D., 2019a. Tuning MnO_2 to FeOOH replicas with bio-template 3D morphology as electrodes for

high performance asymmetric supercapacitors. Chemical Engineering Journal 370, 136-147.

Li, Y., Deng, X., Tian, J., Liang, Z., Cui, H., 2018b. Ti_3C_2 MXene-derived Ti_3C_2/TiO_2 nanoflowers for noble-metal-free photocatalytic overall water splitting. Applied Materials Today 13, 217-227.

Li, Y., Yan, P., Chen, J., Ren, Y., Zhou, Y., Ge, T., Chen, J., Xu, Q., 2019b. High-efficiency electrocatalyst for N_2 conversion to NH_3 based on Au nanoparticles loaded on defective WO_{3-x}. Chemical Communications 55, 13307-13310.

Li, Y., Zhou, X., Luo, W., Cheng, X., Zhu, Y., El-Toni, A.M., Khan, A., Deng, Y., Zhao, D., 2019c. Pore engineering of mesoporous tungsten oxides for ultrasensitive gas sensing. Advanced Materials Interfaces 6, 1801269.

Liu, A., Tai, C.-W., Holá, K., Tian, H., 2019. Hollow polymer dots: nature-mimicking architecture for efficient photocatalytic hydrogen evolution reaction. Journal of Materials Chemistry A 7, 4797-4803.

Mir, R.A., Pandey, O.P., 2019. Waste plastic derived carbon supported Mo_2C composite catalysts for hydrogen production and energy storage applications. Journal of Cleaner Production 218, 644-655.

Nowak, A.P., Sprynskyy, M., Brzozowska, W., Lisowska-Oleksiak, A., 2019. Electrochemical behavior of a composite material containing 3D-structured diatom biosilica. Algal Research 41, 101538.

Patel, M., Kumar, R., Kishor, K., Mlsna, T., Pittman, C.U., Mohan, D., 2019. Pharmaceuticals of emerging concern in aquatic systems: Chemistry, occurrence, effects, and removal methods. Chemical Reviews 119, 3510-3673.

Pervez, S.A., Kim, D., Doh, C.-H., Farooq, U., Choi, H.-Y., Choi, J.-H., 2015. Anodic WO_3 mesosponge@carbon: A novel binder-less electrode for advanced energy storage devices. ACS Applied Materials & Interfaces 7, 7635-7643.

Phang, S.J., Tan, L.-L., 2019. Recent advances in carbon quantum dot (CQD)-based two dimensional materials for photocatalytic applications. Catalysis Science & Technology 9, 5882-5905.

Popkov, V.I., Tolstoy, V.P., Omarov, S.O., Nevedomskiy, V.N., 2019. Enhancement of acidic-basic properties of silica by modification with CeO_2-Fe_2O_3 nanoparticles via successive ionic layer deposition. Applied Surface Science 473, 313-317.

Ragni, R., Cicco, S.R., Vona, D., Farinola, G.M., 2018. Multiple routes to smart nanostructured materials from diatom microalgae: a chemical perspective. Advanced Materials 30, 1704289.

Schneider, J.T., Firak, D.S., Ribeiro, R.R., Peralta-Zamora, P., 2020. Use of scavenger agents in heterogeneous photocatalysis: truths, half-truths, and misinterpretations. Physical Chemistry Chemical Physics 22, 15723-15733.

Shen, Y., Zhang, N., 2019. Facile synthesis of porous carbons from silica-rich rice husk char for volatile organic compounds (VOCs) sorption. Bioresource Technology 282, 294-300.

Singh, R., Singh, A.P., Kumar, S., Giri, B.S., Kim, K.-H., 2019. Antibiotic resistance in major rivers in the world: A systematic review on occurrence, emergence, and management strategies. Journal of Cleaner Production 234, 1484-1505.

Sriram, G., Uthappa, U.T., Rego, R.M., Kigga, M., Kumeria, T., Jung, H.-Y., Kurkuri, M.D., 2020. Ceria decorated porous diatom-xerogel as an effective adsorbent for the efficient removal of Eriochrome Black T. Chemosphere 238, 124692.

Su, S., NuLi, Y., Huang, Z., Miao, Q., Yang, J., Wang, J., 2016. A high-performance rechargeable Mg^{2+}/Li^{+} hybrid battery using one-dimensional mesoporous TiO_2(B) nanoflakes as the cathode. ACS Applied Materials & Interfaces 8, 7111-7117.

Sun, X.-Y., Zhang, F.-J., Kong, C., 2020. Porous g-C_3N_4/WO_3 photocatalyst prepared by simple calcination for efficient hydrogen generation under visible light. Colloids and Surfaces A: Physicochemical and Engineering Aspects 594, 124653.

Sun, Z., Cao, H., Yin, X., Zhang, X., Dong, A., Liu, L., Geng, W., 2018. Precipitation and subsequent preservation of hydrothermal Fe-Mn oxides in distal plume sediments on Juan de Fuca Ridge. Journal of Marine Systems 187, 128-140.

Sun, Z., Jiang, Y., Zeng, L., Huang, L., 2019. Intramolecular charge transfer and extended conjugate effects in donor–π–acceptor-type mesoporous carbon nitride for photocatalytic hydrogen evolution. ChemSusChem 12, 1325-1333.

Teodosiu, C., Gilca, A.-F., Barjoveanu, G., Fiore, S., 2018. Emerging pollutants removal through advanced drinking water treatment: A review on processes and environmental performances assessment. Journal of Cleaner Production 197, 1210-1221.

Tu, J., Lei, H., Yu, Z., Jiao, S., 2018. Ordered WO_{3-x} nanorods: facile synthesis and their electrochemical properties for aluminum-ion batteries. Chemical Communications 54, 1343-1346.

Wan, S., Ou, M., Zhong, Q., Cai, W., 2018. Haloid acid induced carbon nitride semiconductors for enhanced photocatalytic H_2 evolution and reduction of CO_2 under visible light. Carbon 138, 465-474.

Wang, L., Xu, X., Wu, S., Cao, F., 2018. Nonstoichiometric tungsten oxide residing in a 3D nitrogen doped carbon matrix, a composite photocatalyst for oxygen vacancy induced VOC degradation and H_2 production. Catalysis Science & Technology 8, 1366-1374.

744 Wang, Q., Nakabayashi, M., Hisatomi, T., Sun, S., Akiyama, S., Wang, Z., Pan, Z., Xiao, X.,
745 Watanabe, T., Yamada, T., 2019. Oxysulfide photocatalyst for visible-light-driven
746 overall water splitting. Nature materials 18, 827.
747 Wojnárovits, L., Takács, E., Emmi, S.S., 2006. Reaction of the 2-hydroxy-2-propyl radical
748 with acrylate type molecules in aqueous solution: Radical addition or electron transfer.
749 Chemical Physics 327, 335-343.
750 Yan, J., Wang, T., Wu, G., Dai, W., Guan, N., Li, L., Gong, J., 2015. Tungsten oxide single
751 crystal nanosheets for enhanced multichannel solar light harvesting. Advanced
752 Materials 27, 1580-1586.
753 Yang, C., Cheng, J., Chen, Y., Hu, Y., 2017a. CdS nanoparticles immobilized on porous carbon
754 polyhedrons derived from a metal-organic framework with enhanced visible light
755 photocatalytic activity for antibiotic degradation. Applied Surface Science 420, 252-
756 259.
757 Yang, T., Lou, L.-L., Yu, W., Feng, Y., Li, H., Yu, K., Liu, S., 2017b. 3 D ordered macroporous
758 alumina–carbon nanocomposite supported platinum nanoparticles as effective and
759 reusable catalysts for asymmetric hydrogenation. ChemCatChem 9, 458-464.
760 Žerjav, G., Arshad, M.S., Djinović, P., Zavašnik, J., Pintar, A., 2017. Electron trapping energy
761 states of TiO_2–WO_3 composites and their influence on photocatalytic degradation of
762 bisphenol A. Applied Catalysis B: Environmental 209, 273-284.
763 Zhan, F., Liu, Y., Wang, K., Liu, Y., Yang, X., Yang, Y., Qiu, X., Li, W., Li, J., 2019a. In situ
764 formation of WO_3-based heterojunction photoanodes with abundant oxygen vacancies
765 via a novel Microbattery method. ACS Applied Materials & Interfaces 11, 15467-
766 15477.

767 Zhan, F., Liu, Y., Wang, K., Yang, X., Liu, M., Qiu, X., Li, J., Li, W., 2019b. Oxygen-deficient
768 nanofiber WO_{3-x}/WO_3 homojunction photoanodes synthesized via a novel metal self-
769 reducing method. ACS Applied Materials & Interfaces 11, 39951-39960.
770 Zhang, H., Song, Y., Nengzi, L.-c., Gou, J., Li, B., Cheng, X., 2020a. Activation of persulfate
771 by a novel magnetic $CuFe_2O_4/Bi_2O_3$ composite for lomefloxacin degradation. Chemical
772 Engineering Journal 379, 122362.
773 Zhang, J., Ma, Y., Du, Y., Jiang, H., Zhou, D., Dong, S., 2017. Carbon nanodots/WO_3 nanorods
774 Z-scheme composites: Remarkably enhanced photocatalytic performance under broad
775 spectrum. Applied Catalysis B: Environmental 209, 253-264.
776 Zhang, R., Song, C., Kou, M., Yin, P., Jin, X., Wang, L., Deng, Y., Wang, B., Xia, D., Wong,
777 P.K., Ye, L., 2020b. Sterilization of escherichia coli by photothermal synergy of WO_{3-x}/C
778 nanosheet under infrared light irradiation. Environmental Science & Technology
779 54, 3691-3701.
780 Zhang, S., Chen, S., Liu, D., Zhang, J., Peng, T., 2020c. Layered WS_2/WO_3 Z-scheme
781 photocatalyst constructed via an in situ sulfurization of hydrous WO_3 nanoplates for
782 efficient H_2 generation. Applied Surface Science 529, 147013.
783 Zhang, S., Wang, J., Chen, S., Li, R., Peng, T., 2019. Construction of Ag_2S/WO_3 direct Z-
784 scheme photocatalyst for enhanced charge separation efficiency and H_2 generation
785 activity. Industrial & Engineering Chemistry Research 58, 14802-14813.
786 Zhao, S., Li, C., Wang, L., Liu, N., Qiao, S., Liu, B., Huang, H., Liu, Y., Kang, Z., 2016.
787 Carbon quantum dots modified MoS_2 with visible-light-induced high hydrogen
788 evolution catalytic ability. Carbon 99, 599-606.
789 Zhao, X., Zhang, X., Han, D., Niu, L., 2020. Ag supported Z-scheme $WO_{2.9}$/g-C_3N_4 composite
790 photocatalyst for photocatalytic degradation under visible light. Applied Surface
791 Science 501, 144258.

Zhou, Y., Wang, N., Qu, X., Huang, F., Duan, Y., Zhang, X., Dong, X., Zhang, Z., 2019. Arc-discharge synthesis of nitrogen-doped C embedded TiCN nanocubes with tunable dielectric/magnetic properties for electromagnetic absorbing applications. Nanoscale 11, 19994-20005.

Appendix

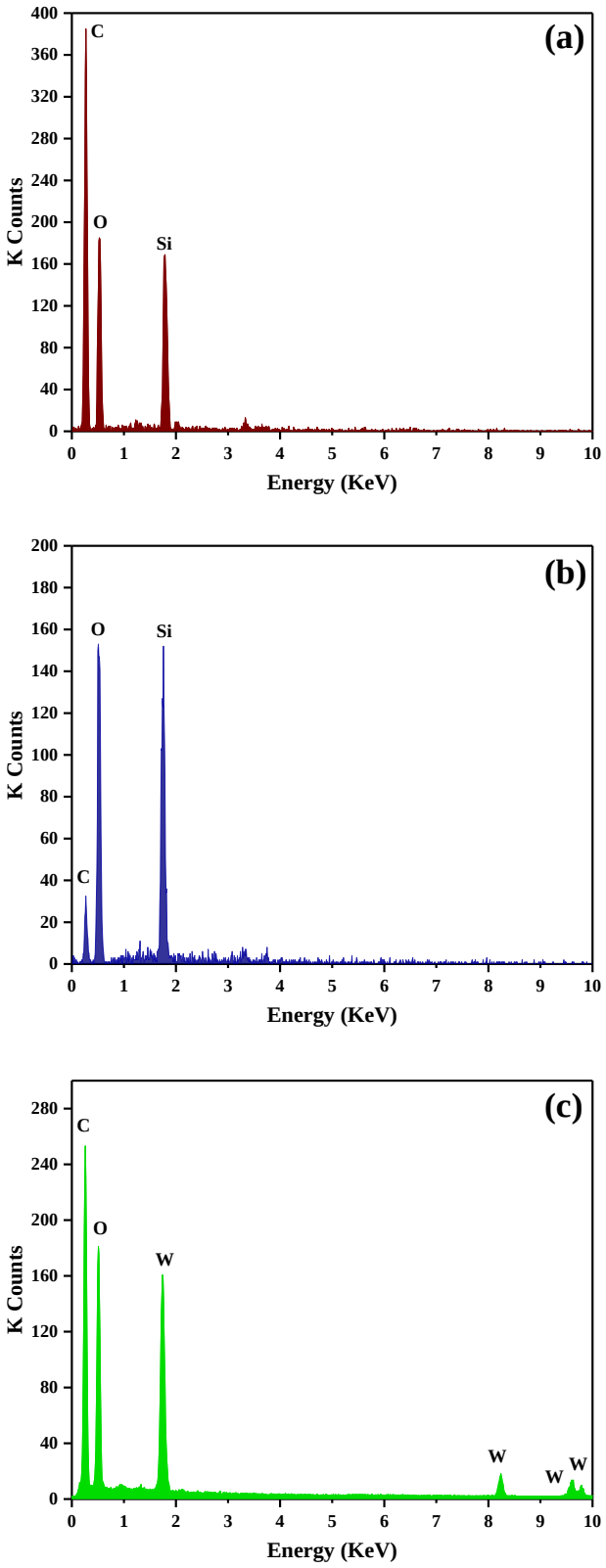

Fig. A1. EDS spectra of untreated frustule (a), treated frustule (b) and DT-WO_{3-x}@MC nanohybrid (c)

Table A1. Textural characteristics of the samples.

Sample	Surface area ($m^2 g^{-1}$)	Total pore volume ($cm^3 g^{-1}$)	Pore size (nm)
Diatom frustules	132.67	0.18	18.13
WO_3	87.52	0.10	11.42
DT-WO_{3-x}@MC	195.37	0.39	6.59

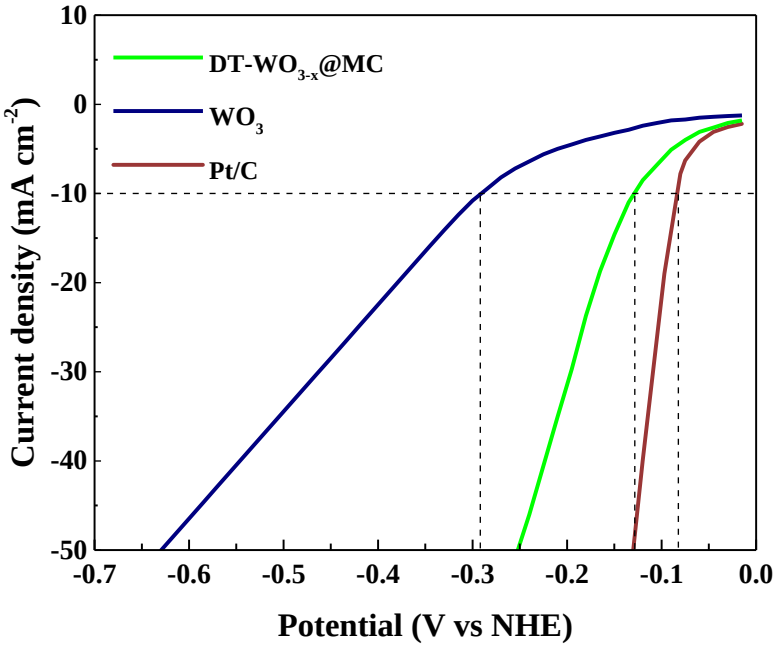

Fig. A2. Comparison of LSV curves of WO_3 and DT-WO_{3-x}@MC coated GCE electrodes with that of commercial Pt/C electrode.

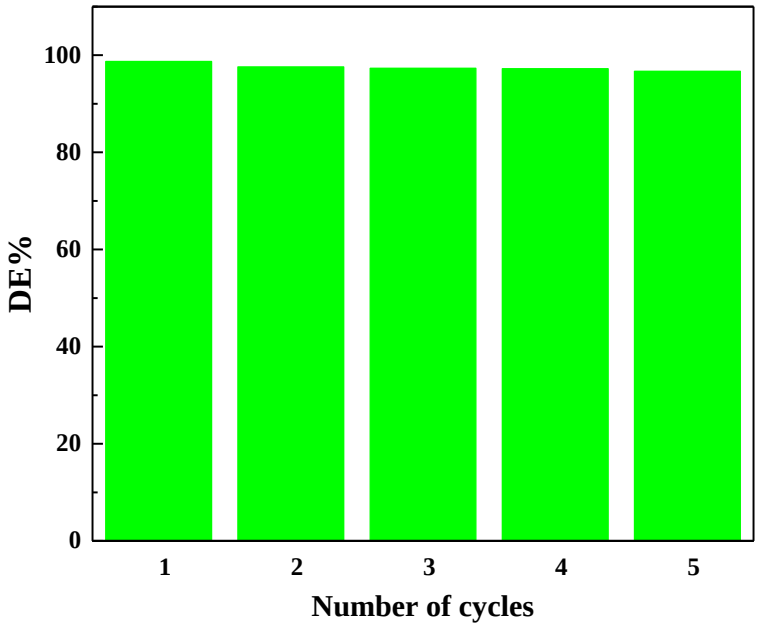

Fig. A3. Cyclic stability of DT-WO_{3-x}@MC nanohybrid for degradation of CFZ under visible light irradiation; Experimental condition: [photocatalyst] = 0.6 g L^{-1}, [CFZ] = 3 mM, pH = 6.3 and temperature = 30±1 °C.

882

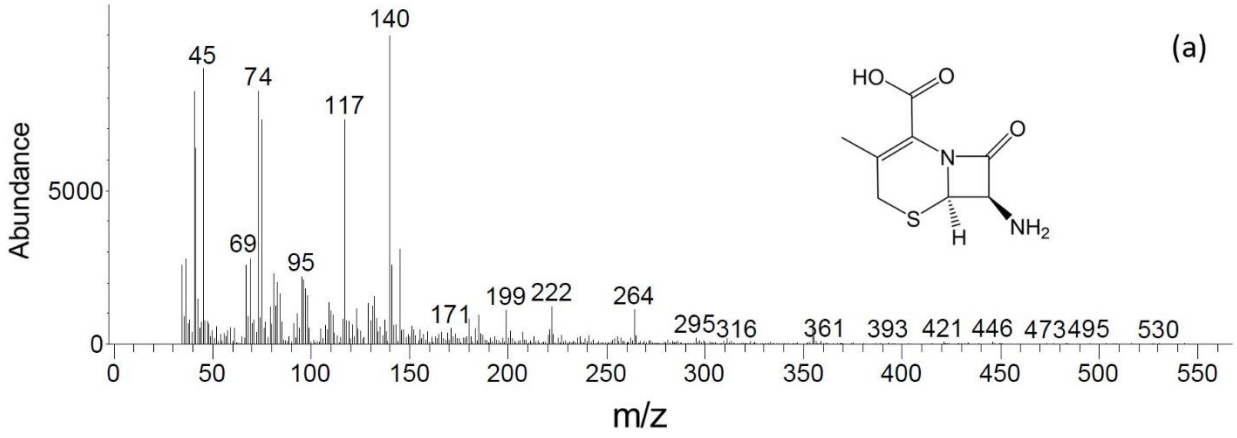

883

884

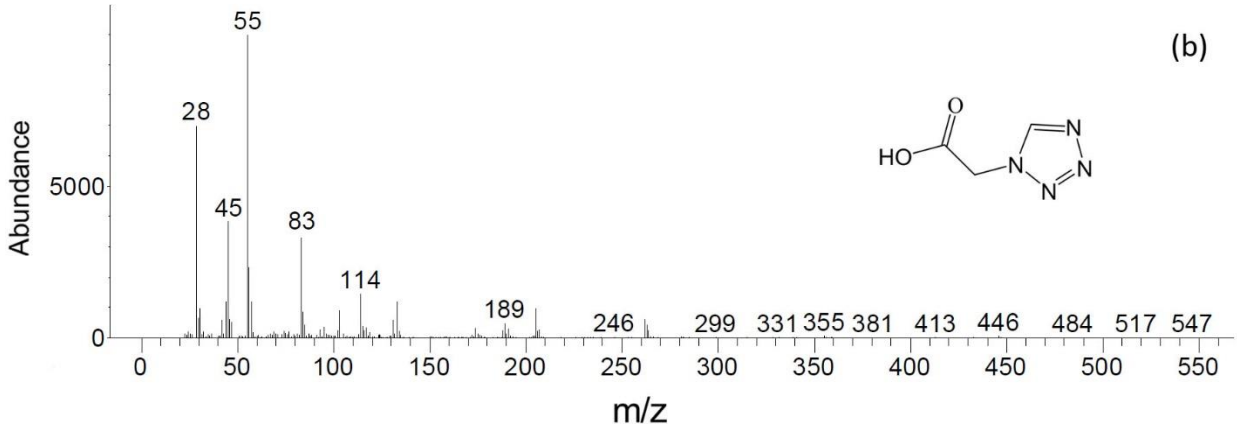

885

886

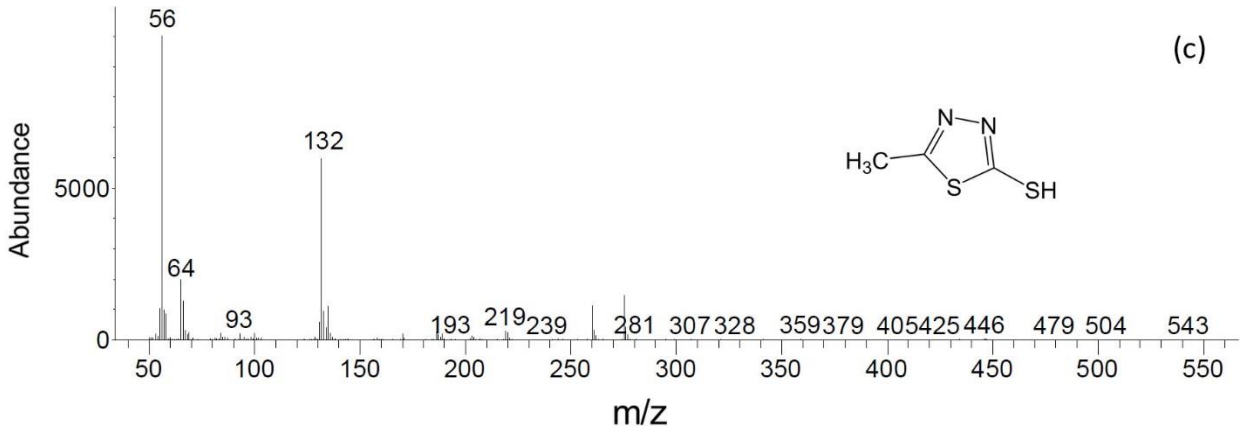

887

888

889

890

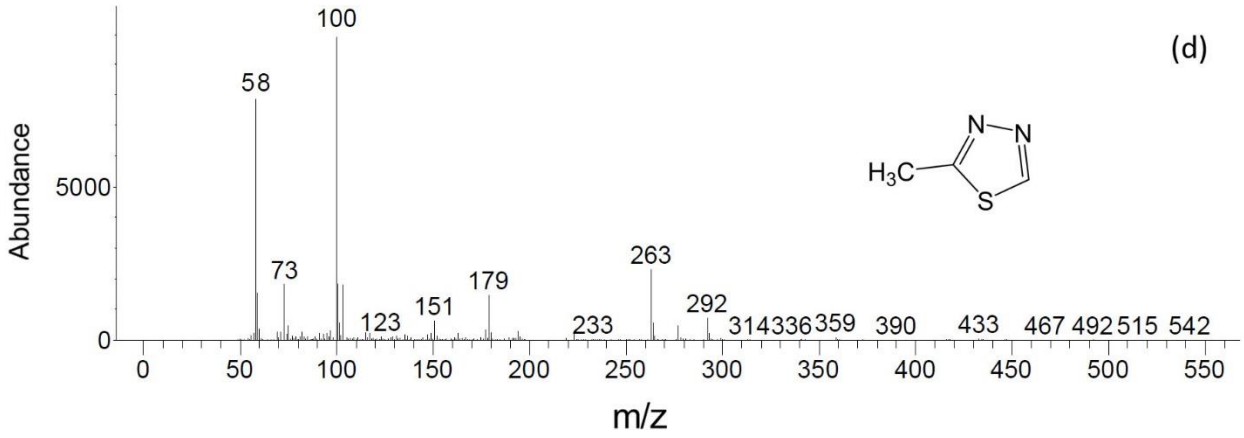

891

892

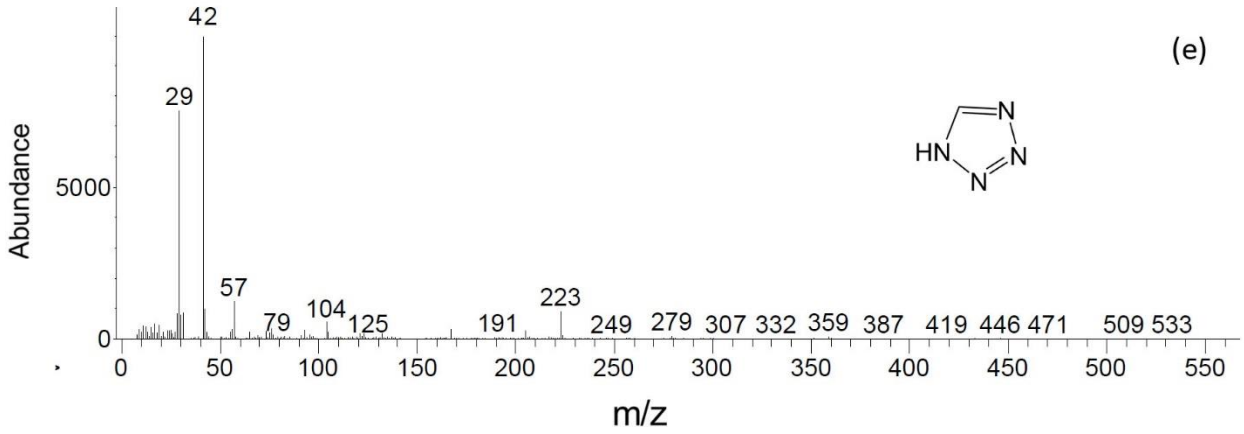

893

894

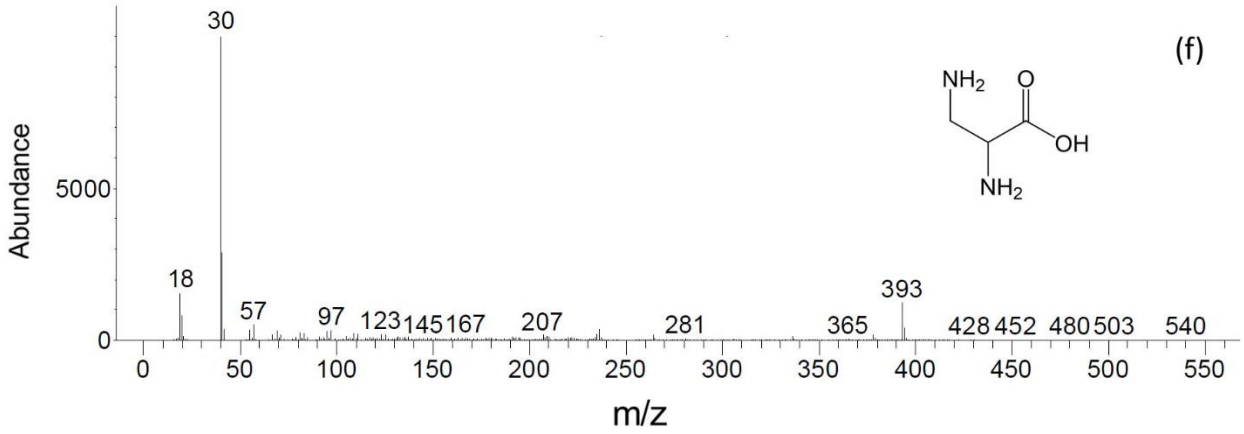

895

896

897

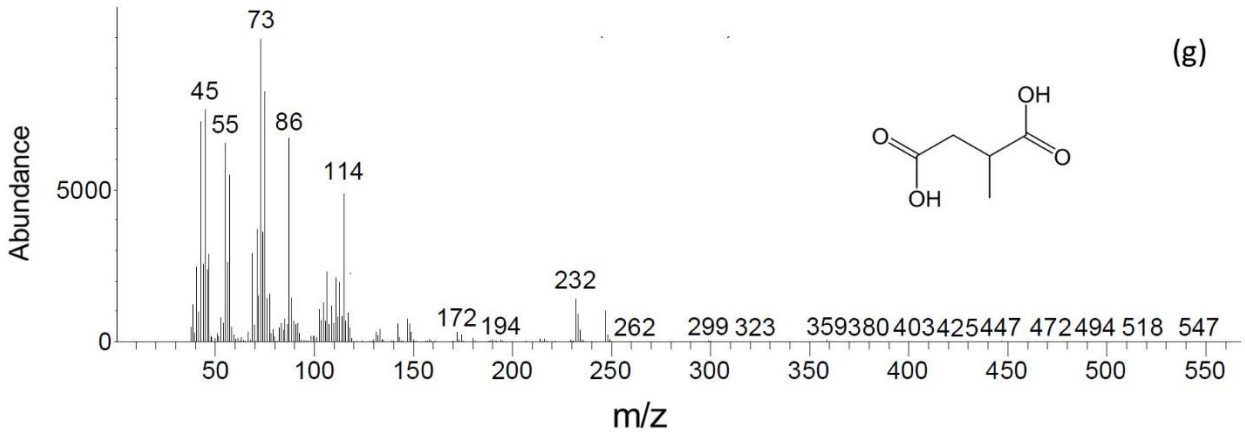

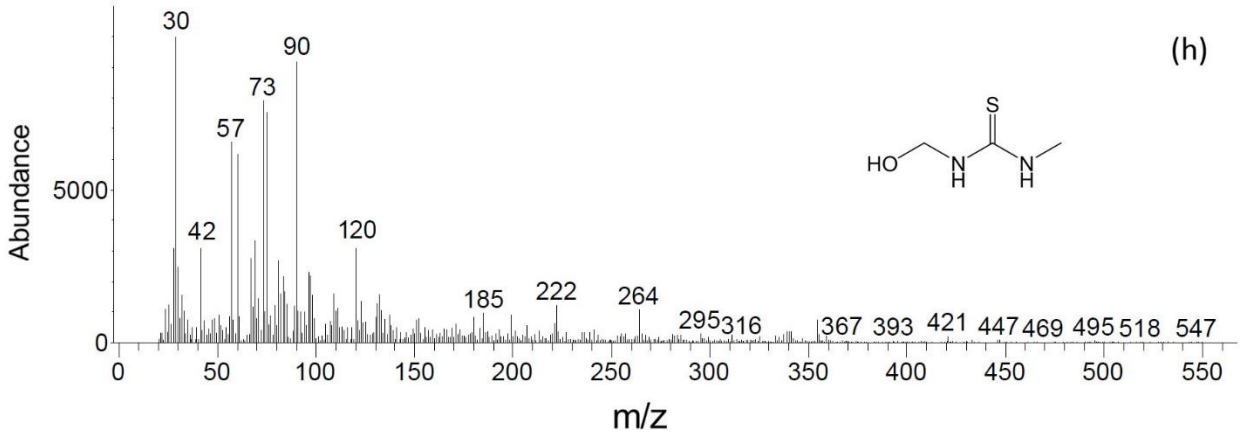

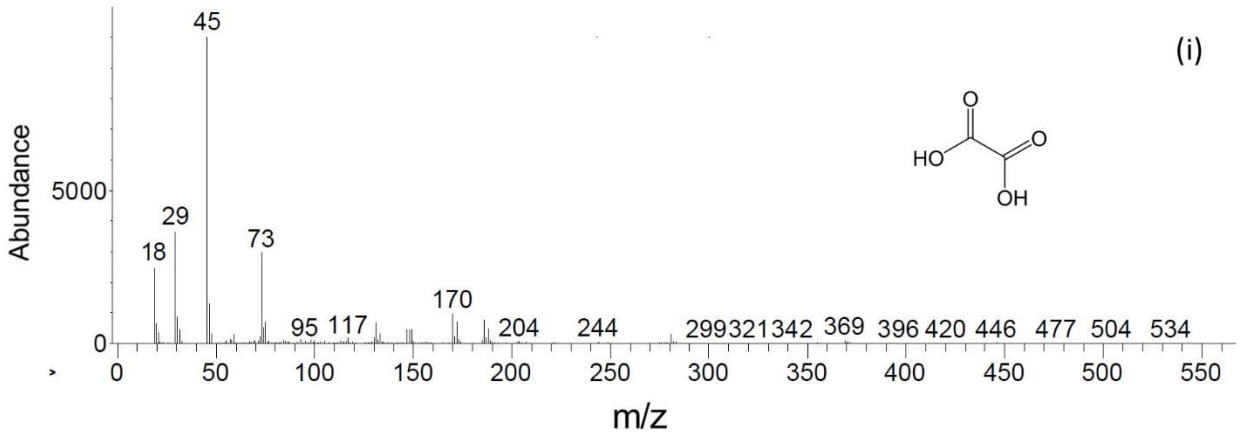

Fig. A4. GC-MS spectra of intermediates and their structures (a-i).

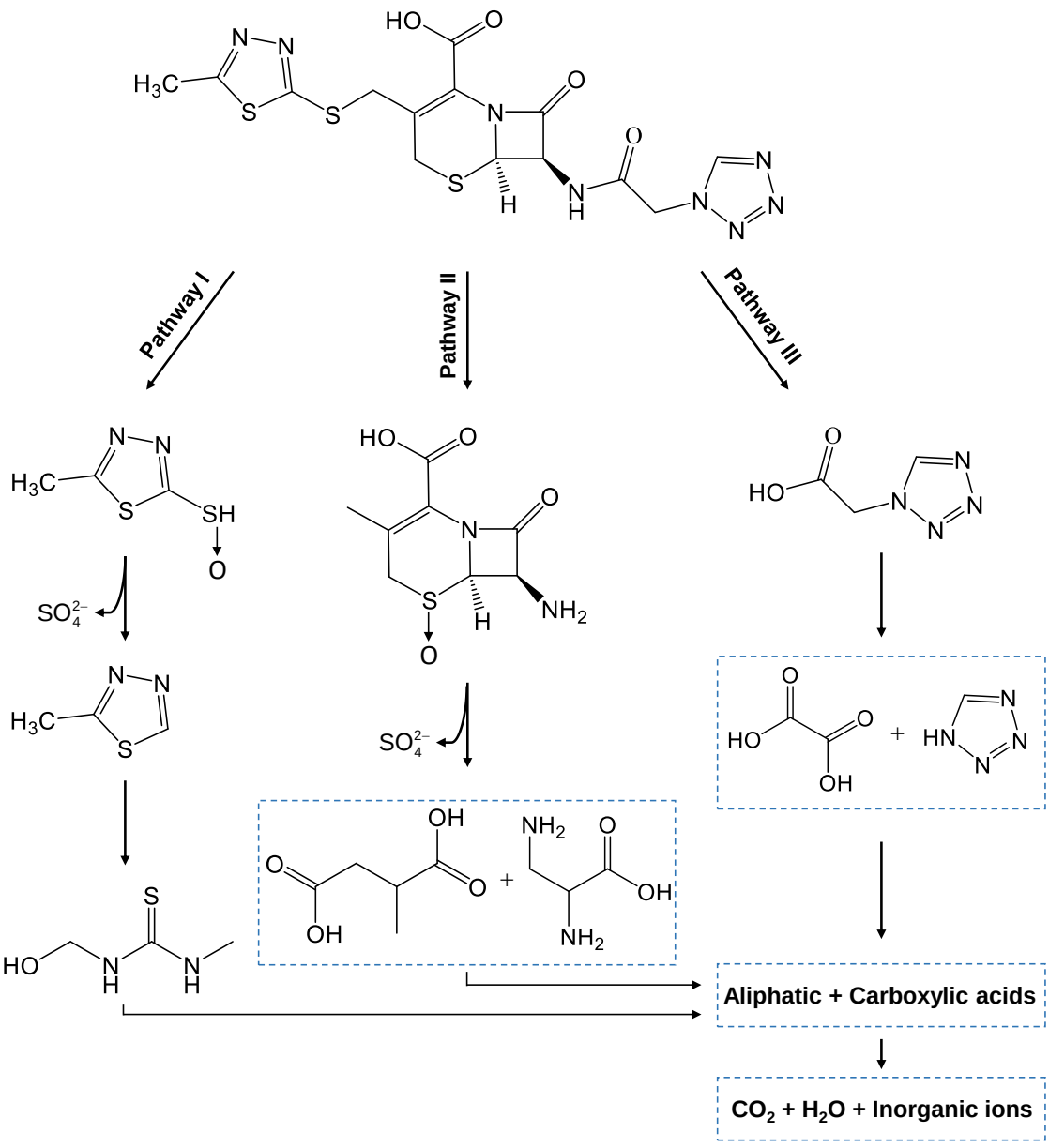

Fig. A5. The proposed pathways for the photodegradation of CFZ using DT-WO_{3-x}@MC photocatalyst under visible light irradiation.

Graphical Abstract

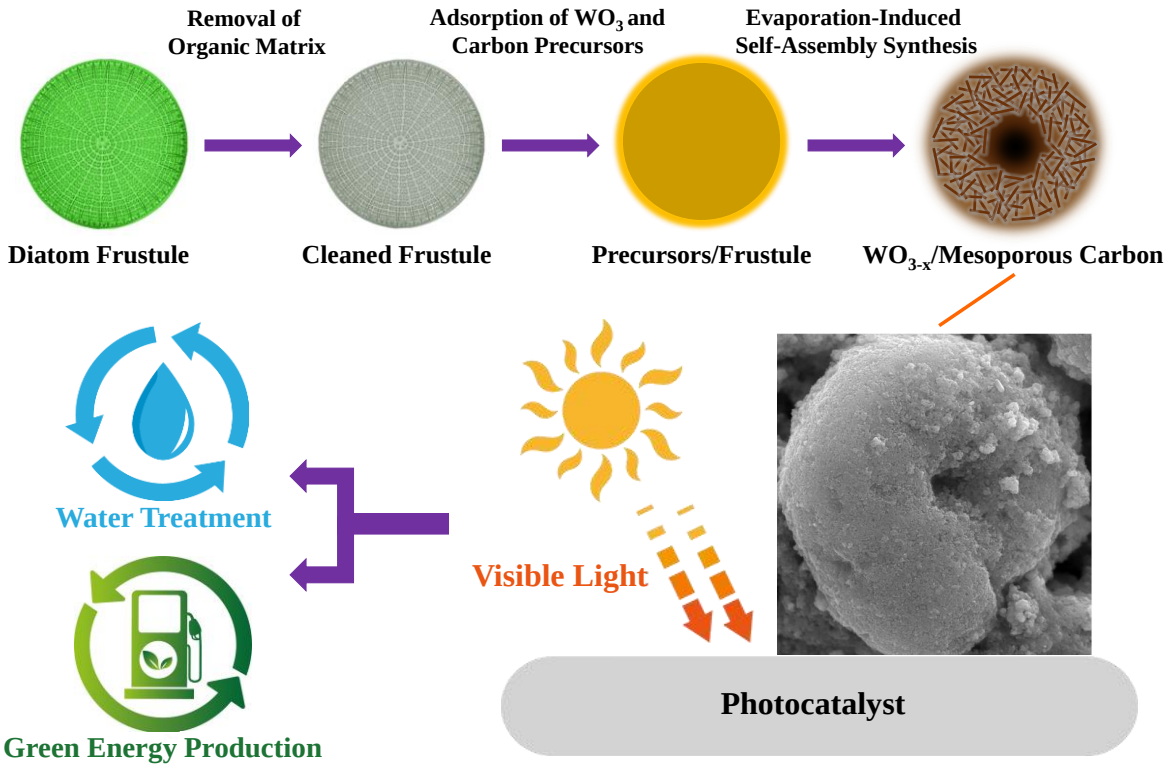

Evaporation-induced self-assembly synthesis of WO_{3-x}@MC nanohybrid using diatom template for photocatalytic H_2 production and water treatment.

Research highlights

- Synthesis of 3D reduced tungsten oxide@mesoporous carbon using diatom template.
- Superior photocatalytic properties of synthesized nanohybrid compared to pure WO_3.
- Photocatalytic cefazolin degradation and H_2 production using synthesized nanohybrids.
- Reusability of tungsten oxide@mesoporous carbon photocatalyst after five cycles.
- A possible pathway for cefazolin photodegradation.